

Article

Ore Genesis and the Magmatism of the Yuhaixi Mo(Cu) Deposit in Eastern Tianshan, NW China: Constraints from Geology, Geochemistry, Zircon U-Pb and Molybdenite Re-Os Dating

Di Wang ^{1,2}, Chunji Xue ^{1,3,*}, Yun Zhao ¹, Chao Li ^{2,*}, Binbin Xi ⁴, Yang Yang ⁴, Qinglei Tian ⁴, Xunshan Kang ⁴ and Xing Wu ⁴

¹ State Key Laboratory of Geological Processes and Mineral Resources, China University of Geosciences, Beijing 100083, China; shadywangdi@gmail.com (D.W.); yun.zhao@cugb.edu.cn (Y.Z.)

² National Research Center for Geoanalysis, Beijing 100037, China

³ The National 305 Project Office of Xinjiang, Urumqi 830000, China

⁴ No. 704 Geological Party, Xinjiang Geological Exploration Bureau for Nonferrous Metals, Hami 839005, China

* Correspondence: chunji.xue@cugb.edu.cn (C.X.); re-os@163.com (C.L.)

Abstract: The Yuhaixi Mo(Cu) deposit is a new discovery in the eastern section of the Dananhu-Tousuquan island arc, Eastern Tianshan. However, the genesis of the Yuhaixi Mo(Cu) deposit is still not fully understood. The Yuhaixi intrusion is composed of monzonitic granites, diorites, granites, and gabbro dikes, among which disseminated or veinlet Mo and Cu mineralization is mainly hosted by the monzonitic granites. The LA-ICP-MS zircon U-Pb dating yields emplacement ages of 359.4 ± 1.6 Ma for the monzonitic granite, 298.8 ± 1.8 Ma for the diorite, and 307.0 ± 2.3 Ma for the granite. The Re-Os dating of molybdenite hosted by monzonitic granite yields a well-constrained ^{187}Re - ^{187}Os isochron age of 354.1 ± 6.8 Ma (MSWD = 1.7) with a weighted average age of 344.5 ± 3.1 Ma. The Mo mineralization is closely associated with the Yuhaixi monzonitic granite. The Yuhaixi monzonitic granite rocks are characterized by high silica ($\text{SiO}_2 > 70$ wt.%), low MgO (0.23–0.36), Ni, Cr contents, and they are enriched in light rare earth elements (LREEs) and large ion lithophile elements (LILEs: e.g., K, Ba, Pb and Sr), and depleted in heavy rare earth elements (HREEs) and high field-strength elements (HFSEs: e.g., Nb, Ta and Ti). They are weak peraluminous and have high $\epsilon\text{Hf}(t)$ (11.37–17.59) and $\epsilon\text{Nd}(t)$ (1.36–7.75) values, and varied initial $^{87}\text{Sr}/^{86}\text{Sr}$ (0.7037–0.7128) values. The Yuhaixi post-ore granites exhibit similar geochemical and isotopic signatures to the Yuhaixi monzonitic granite. These characteristics suggest that the Yuhaixi felsic rocks are likely sourced from the partial melting of the juvenile lower crust. The Yuhaixi diorite has low SiO_2 , and K_2O contents, relatively high Na_2O , MgO ($\text{Mg}^\# = 45$ –53) contents, and depletions in HFSE (e.g., Nb, Ta, and Ti). These geochemical features, coupled with isotopic data such as low initial $^{87}\text{Sr}/^{86}\text{Sr}$ (≤ 0.7043), high $\epsilon\text{Nd}(t)$ (2.5 to 3.0) and $\epsilon\text{Hf}(t)$ (≥ 11.6) values, and young Hf model ages, suggest that their parental magmas possibly originated from the partial melting of the depleted lithospheric mantle that was metasomatized by hydrous melts or fluids from the subducting oceanic plate. Integrating our new results with previous works on the Dananhu-Tousuquan island arc belt, we suggest that the Yuhaixi Mo(Cu) deposit is likely sourced from the juvenile lower crust, which was formed in an arc setting, where the bipolar subduction of the North Tianshan oceanic slab forms the Dananhu Tousuquan belt to the north and the Aqishan-Yamansu belt to the south. The eastern section of the Dananhu-Tousuquan island arc is a promising target for late Paleozoic porphyry Mo(Cu) deposits.

Keywords: LA-ICP-MS zircon U-Pb dating; geochemistry; Sr-Nd-Hf isotope; molybdenite Re-Os dating; Yuhaixi Mo deposit; Eastern Tianshan



Citation: Wang, D.; Xue, C.; Zhao, Y.; Li, C.; Xi, B.; Yang, Y.; Tian, Q.; Kang, X.; Wu, X. Ore Genesis and the Magmatism of the Yuhaixi Mo(Cu) Deposit in Eastern Tianshan, NW China: Constraints from Geology, Geochemistry, Zircon U-Pb and Molybdenite Re-Os Dating. *Minerals* **2023**, *13*, 1368. <https://doi.org/10.3390/min13111368>

Academic Editor: Alain Chauvet

Received: 22 August 2023

Revised: 15 October 2023

Accepted: 21 October 2023

Published: 26 October 2023



Copyright: © 2023 by the authors. Licensee MDPI, Basel, Switzerland. This article is an open access article distributed under the terms and conditions of the Creative Commons Attribution (CC BY) license (<https://creativecommons.org/licenses/by/4.0/>).

1. Introduction

Porphyry ore deposits are the primary source of Cu, Mo, and Au [1–3]. Porphyry-type deposits commonly form in the young continental and oceanic arcs [4], and they are

usually associated with magmatic–hydrothermal fluids exsolved from relatively oxidized intermediate-felsic magmas with high oxidation states [1,4]. However, porphyry Mo(Cu) deposits in the margins of North China Craton mainly occurred in a post-collision extension setting and the ore-forming magmas stemmed from an old lower crust source [5–14]. Therefore, the origin and evolution processes of ore-forming magmas and their tectonic setting are significant for understanding the formation of economic porphyry deposits [1,2,4].

Recently, numerous early Paleozoic porphyry Cu-Mo deposits have been discovered in the Eastern Tianshan, southern margin of the Central Asian Orogenic Belt (CAOB). These porphyry-type deposits are closely related to the Paleozoic intermediate to felsic magmatic hydrothermal activity in the Eastern Tianshan [15–17]. The Dananhu-Tousuquan arc belt (DTA) is located in the northern part of the Eastern Tianshan, which hosts Tuwu-Yandong, Fuxing, Linglong, Chihu, Yuhai porphyry deposits. Previous studies are mainly focused on these porphyry deposits in the middle section, which have revealed that most of the porphyry Cu-Mo deposits were likely related to the subduction of the North Tianshan Oceanic plate in the late Paleozoic [4–10]. However, the genesis of the porphyry Mo(Cu) deposits in the eastern section of the DTA has not been fully understood.

The Yuhaixi porphyry Mo(Cu) deposit is a new discovery in the eastern section of the DTA, which provides a good opportunity for investigating the generation mechanisms for the porphyry Mo deposits in this section [10–14]. In this study, zircon LA-ICP-MS U-Pb dating and trace elements, zircon Hf isotope compositions, whole-rock geochemical data, and molybdenite Re-Os isotope dating were carried out to constrain the magma origins and the timing of mineralization in the Yuhaixi Mo(Cu) deposit. This study provides new insights on the evolution of the DTA and its potential for porphyry Mo(Cu) mineralization in Eastern Tianshan.

2. Geological Settings

2.1. Regional Geology

The CAOB, which is placed between the European and Siberian Cratons in the north and the North China and Tarim Cratons in the south, is the largest Phanerozoic accretionary orogenic belt in the world [8]. The west–east trending Eastern Tianshan orogenic belt is situated in the southern margin of the CAOB. The Eastern Tianshan is a Paleozoic island arc system, which is located between the Jungar Basin and the Tarim Craton (Figure 1), characterized by a series of complicated tectonic history, which has witnessed multiple stages of subduction and collisional events [11–17]. It can be divided into three major tectonic zones from the north to the south: the Bogeda-Haerlike belt, the Jueluotage belt, and the Central Tianshan block (Figure 1c). The Eastern Tianshan belt withstands a series of E–W trending faults, including the Kanggur, the Yamansu, the Dacootan, and the Aqikekuduke faults [12]. The Dananhu-Tousuquan island arc belt mainly consists of Devonian to Carboniferous sedimentary–volcanic rocks. The Devonian Dananhu Formation consists of basaltic to andesitic volcanic rocks, which were overlain by the Carboniferous Gandun Formation sedimentary rocks and Qie’shan Group basaltic–andesitic volcanic/pyroclastic rocks and sedimentary rocks. Most of the Cu-Mo deposits in the Eastern Tianshan porphyry are hosted in the middle section of the Dananhu-Tousuquan island arc belt [15,18–25]. The Kangguer shear zone mainly comprises volcanic–sedimentary rocks of the Carboniferous Gandun and Wutongwozi formations, and volcanic and pyroclastic rocks of the Carboniferous Yamansu Formation [15,16]. Most rocks were metamorphosed and ductile deformed in the Kangguer shear zone [11,15]. The Aqishan-Yamansu belt comprises bimodal volcanic rocks of the Carboniferous Yamansu Formation, as well as clastic rocks, andesitic tuff, and the Permian Kula Formation marine and terrestrial clastic rocks [15,25–29].

2.2. Ore Deposit Geology

The Yuhaixi Mo(Cu) deposit is located in the eastern section of the Dananhu-Tousuquan arc belt, approximately 110 km southeast of Hami City, Xinjiang (Figure 1b). The main lithostratigraphic units in the area include granulite, hornblende schist of the lower Carboniferous

Yanchi Formation, and glutenite of the Tertiary Putaogou Formation (Figure 2A; [5]). The intrusive complex at Yuhaixi is intermediate to felsic in composition (Figure 2B). In the middle and eastern area, various granitoid intrusions occur as stocks and dikes that cover an area of approximately 3 km². These intrusions are composed of monzonitic granite, granite, diorite (Figure 2B). The monzonitic granites host most of the Mo and Cu mineralization at Yuhaixi. Postmineralization plutons comprising granite and diorite intruded the mineralized monzonitic granite. The gabbro dikes mark the final stage of magmatic activity, having intruded the monzonitic granite and the Yanchi Formation (Figure 2B). In the study area, the monzonitic granite and granite generally exhibit low or moderate degrees of alteration. The monzonitic granite is primarily composed of plagioclase (~25%), K-feldspar (~35%), quartz (~25%), and biotite (~5%), with accessory apatite and zircon (Figure 4A,D). The diorite is light gray to gray-white in color and has a microgranular or aphanitic groundmass. It mainly consists of plagioclase (~45%), hornblende (~20%), quartz (~15%), and biotite (~15%), with minor accessory minerals (Figure 4B,E). The granite is coarse-grained and shows typical equigranular texture. It consists of plagioclase (~35%), quartz (~30%), and biotite (~5%), with negligible magnetite, apatite, and zircon (Figure 4C,F). The Yuhaixi intrusive complex has been affected by subordinate faults associated with the regional-scale Kanggur fault [27–37]. The early NE-trending fault dips 65° to 85° and is inferred to be the predominant structure in the Yuhaixi area (Figure 2A). Geologic surveying defined that the ore zone consists of 6 orebodies, which is based on the drill hole ZK3201 and ZK3601. Each individual orebody is about 2–10 m thick (Figure 3A,B). The monzonitic granite have a genetic relationship with disseminated molybdenite and chalcopyrite (Figure 4G–I) and associated hydrothermal alterations (Figure 4I–K).

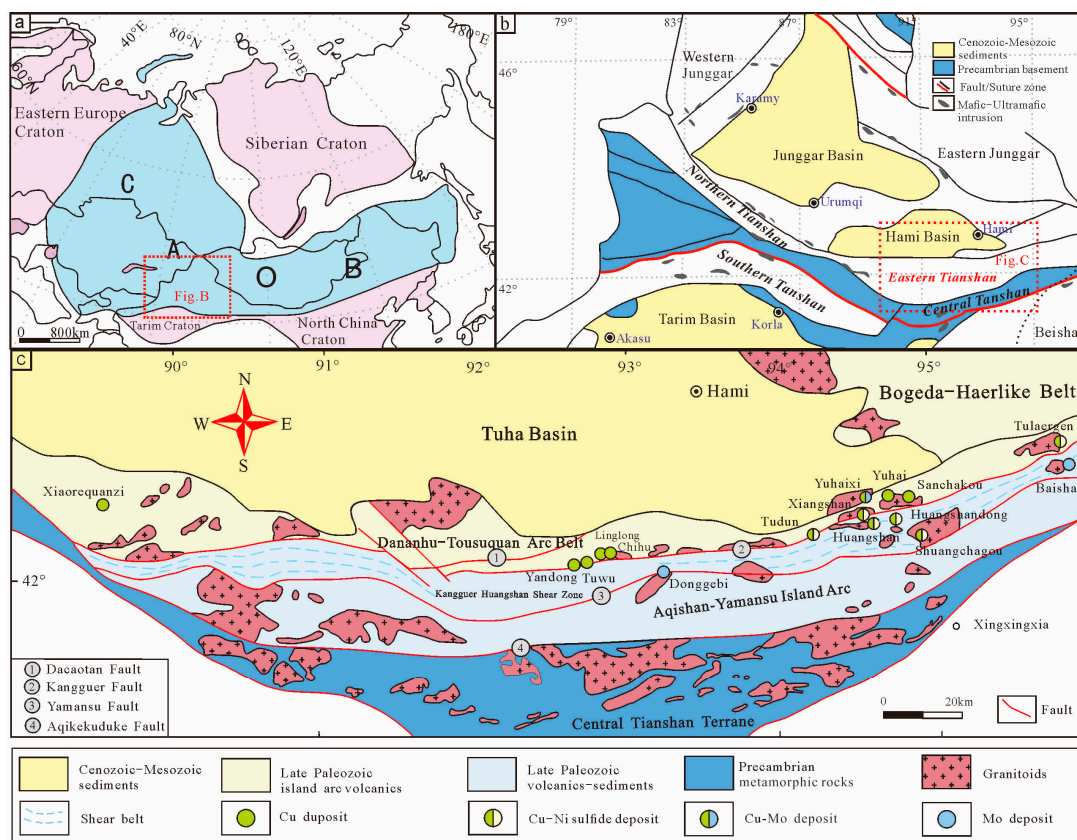


Figure 1. (a) Location of Central Asian Orogenic Belt (CAOB) [4]; (b) geological map of NW China showing the main tectonic units; (c) geological map of Eastern Tianshan showing major tectonic units, faults and copper deposits (modified from [12]).

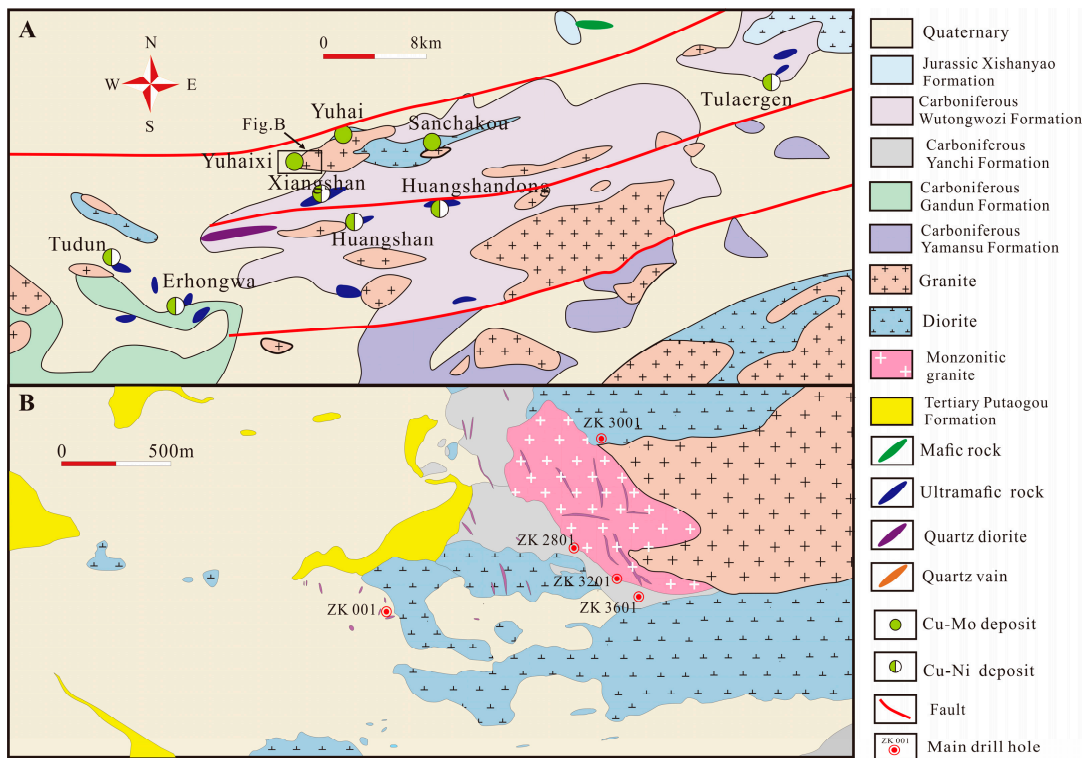


Figure 2. (A) Geological map of the Yuhai region showing the distribution of Cu and Cu-Ni deposits. (B) Simplified geological map of the Yuhai Mo(Cu) deposit (modified from [30]).

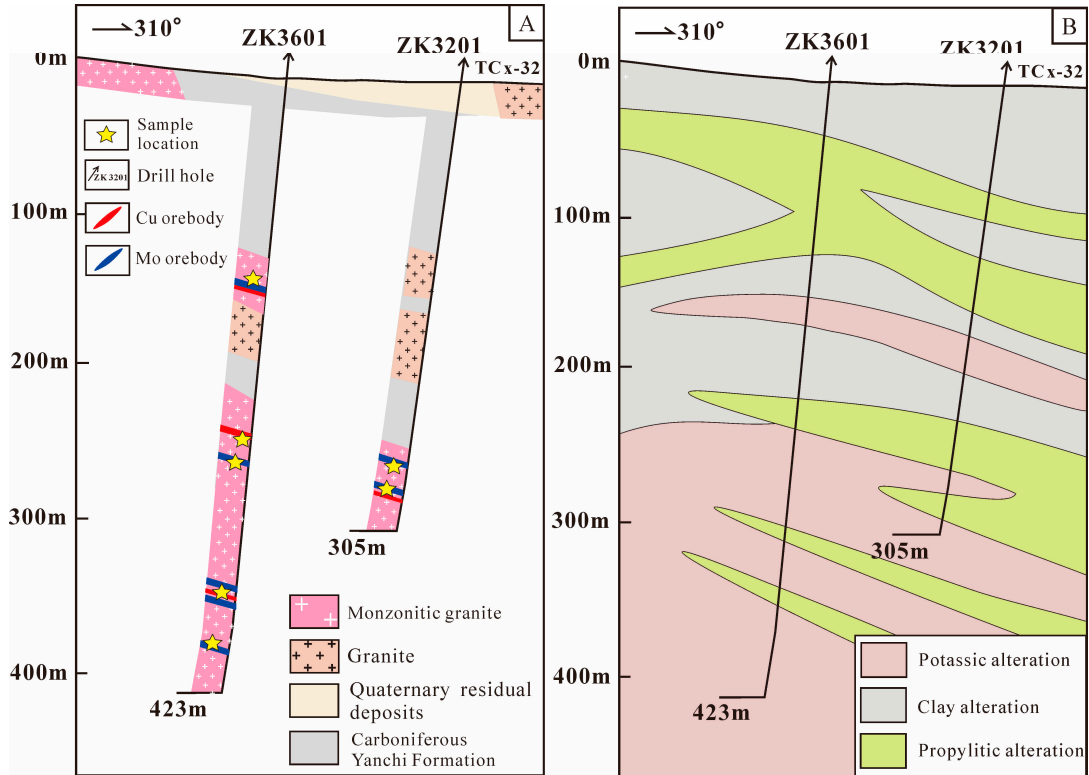


Figure 3. Geologic cross section of the ZK3601 and ZK3201 exploration lines across the Yuhai porphyry Mo deposit with lithology and mineralization (A) and alteration (B).

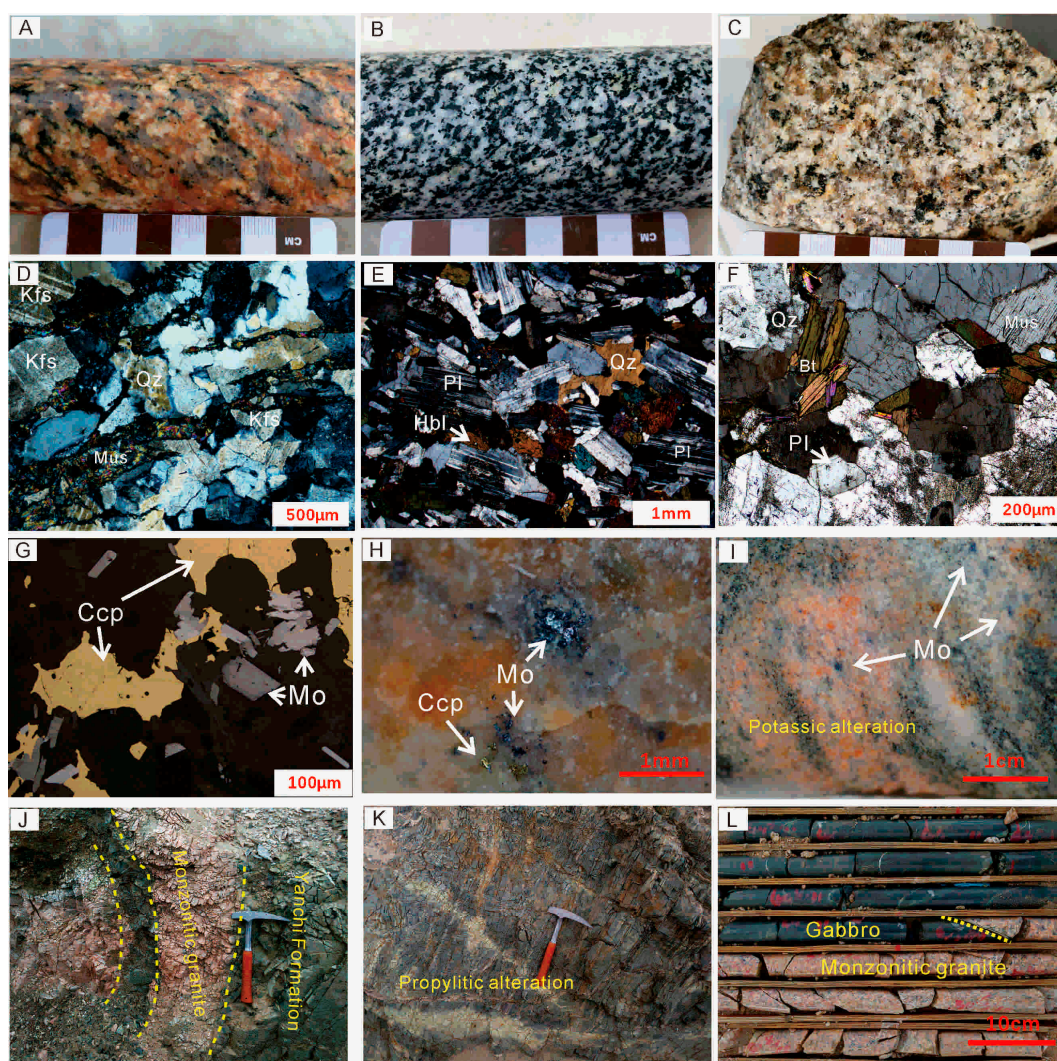


Figure 4. Field, hand specimen, and microscope photos of magmatic intrusions in the Yuhaixi area. (A–C) Hand specimen of the monzonitic granite (A), diorite (B), granite (C). (D) Photomicrograph of the monzonitic granite, showing K-feldspar, quartz, and muscovite phenocrysts under cross-polarized light. (E) Photomicrograph of the diorite, showing plagioclase, quartz, and hornblende phenocrysts under cross-polarized light. (F) Photomicrograph of the granite, showing biotite, quartz, and plagioclase phenocrysts under cross-polarized light. (G) Photomicrograph of the anhedral chalcopyrite and euhedral molybdenite assemblages under reflected light. Abbreviations: Group; Qtz, quartz; Pl, plagioclase; Bt, biotite; Mus, muscovite; Kfs, K-feldspar; Ccp, chalcopyrite; Mo, molybdenite. (H,I) The molybdenite in the monzonitic granite hand specimen, with potassic alteration. (J) The Carboniferous Yanchi Formation rocks and the monzonitic granite in the exploratory trench. (K) Propylitic alteration in the exploratory trench. (L) The gabbro dike intruded into early monzonitic granite.

3. Materials and Methods

3.1. Sampling

Three representative intrusive samples (YHX-ZK-1, ZK001-412, 721-6) from the Yuhaixi outcrops (granite) and drill holes (monzonitic granite, diorite) were collected for zircon LA-ICP-MS U-Pb dating, trace element and Hf isotope analyses. Nine samples, including monzonitic granite (Sample No. YHX-ZK-14, YHX-ZK2, YHX-ZK3), diorite (Sample No. ZK001-25, ZK001-350, ZK001-396), and granite (Sample No. 721-1, 721-3, 721-5), were chosen for major and trace element analysis and Sr-Nd isotope analyses. In addition, nine

molybdenite samples from Mo orebodies of the Yuhaixi deposit were collected from the disseminated ores for Re-Os isotope analyses.

3.2. Zircon U-Pb Dating and Trace Elements

Three samples, including one monzonitic granite (sample YHX-ZK-1), one diorite (sample ZK001-1), and one granite (721-6), were chosen for the zircon LA-ICP-MS U-Pb dating and trace element analysis.

The zircon grains were separated by conventional density and magnetic techniques and then carefully hand-picked under a binocular microscope. Subsequently, they were mounted on epoxy resin discs and polished to expose the crystal cross-sections at the Langfang Regional Geological Survey. The selection of potential target sites for the U-Pb dating of all the mounted zircons were based on photomicrographs of both transmitted and reflected light, as well as cathodoluminescence (CL) images. Zircon U-Pb dating and trace element analyses were conducted using an Agilent 7500 a inductively coupled plasma mass spectrometer (ICP-MS) simultaneously coupled with a GeoLas 2005 at the Tianjin Institute of Geology and Mineral Resources. The analytical procedures were described in [38]. Laser ablation was operated at a constant energy of 60 mJ, with a repetition rate of 4 Hz and a spot diameter of 32 μm . Zircons 91500 and GJ-1, NIST SRM 610 [30] were used as external standards. Zircon 91500 was analyzed twice for every six analyses in order to calibrate the isotope fractionation. NIST SRM 610 was analyzed once every eight analyses to make the instrumental drift and mass discrimination correction of the trace element analysis. Individual errors in analyses were cited at the 1σ level, and the weighted mean $^{206}\text{Pb}/^{238}\text{U}$ ages were quoted at the 95% confidence level. The ICPMSDataCal software GeoLas 2005 were used for the adjustment of background and ablation signals, time drift correction [38]. Concordia diagrams and weighted mean calculations were determined using Isoplot 3.0 [39]. Zircon Ce anomalies were calculated using the method of the lattice strain model [17].

3.3. Zircon Hf Isotopes

In situ Hf isotope analyses were conducted using a Neptune MC-ICP-MS and New Wave UP 213 ultraviolet LA-MC-ICP-MS at the National Research Center for Geoanalysis, Beijing, China. The analysis was undertaken on the adjacent spots used for the LA-ICP-MS zircon U-Pb dating to match the Hf isotope data with the U-Pb ages. The ablated samples wrapped in helium were transported from the laser ablation chamber to the ICP-MS torch via a mixing chamber of Argon. Based on the zircon size, the stationary beam spot size was set to either 40 or 50 μm . During testing, GJ-1 international standard [30] zircon samples were used as a reference for the instrumental mass bias correction. The weighted average of the $^{176}\text{Hf}/^{177}\text{Hf}$ of the GJ-1 zircon samples was 0.281017 ± 0.000007 (2 SD, $n = 10$), which is consistent with the values reported by [18]. More detailed operating conditions for the MC-ICP-MS instrument, the laser ablation system, and the analytical method are given in [39,40].

3.4. Whole-Rock Major and Trace Elements

Whole-rock major and trace elements analyses were performed at the National Research Center for Geoanalysis, Beijing, China. The samples were powdered to approximately 200 mesh before testing. The major elements were determined using a Philips PW 2404 X-ray fluorescence (XRF) spectrometer with a rhodium X-ray source. The trace elements and the rare earth elements were determined using an Element-I plasma mass spectrometer (Finnigan-MAT Ltd., Bremen, German); two national geological standard reference samples, GSR-3 and GSR-15, were used for the analytical quality control purpose. The analytical precision for the major elements is better than 1% and for the trace elements is better than 5%, and the analytical procedures were described by [19].

3.5. Whole-Rock Sr-Nd Isotopes

Sr–Nd isotopic analyses were carried out using a Neptune multi-collector ICP–MS at the National Research Center for Geoanalysis, Beijing, China, using analytical procedures described by [40]. The Separation of the Sr and REE were performed using cation columns, and the Nd fractions were further separated using HDEHP-coated Kef columns. The measured $^{87}\text{Sr}/^{86}\text{Sr}$ and $^{143}\text{Nd}/^{144}\text{Nd}$ ratios were normalized to $^{86}\text{Sr}/^{88}\text{Sr} = 0.1193$ and $^{146}\text{Nd}/^{144}\text{Nd} = 0.7217$, respectively. The reported $^{87}\text{Sr}/^{86}\text{Sr}$ and $^{143}\text{Nd}/^{144}\text{Nd}$ ratios were adjusted to the NBS SRM 987 standard $^{87}\text{Sr}/^{86}\text{Sr} = 0.71027$ and the Shin Etsu JNdi-1 standard $^{143}\text{Nd}/^{144}\text{Nd} = 0.512116$ [11], respectively.

3.6. Re-Os Isotopic Analyses

Nine molybdenite samples were collected from the Yuhaixi porphyry Mo(Cu) deposits for Re–Os isotope analyses. Among them, five molybdenite samples came from drill holes ZK3601. Four molybdenite samples came from drill hole ZK3201. The photographs and photomicrographs of the representative samples are shown in Figure 4. Molybdenite occurs as disseminations in monzonitic granite or quartz veinlets and molybdenite is cogenetic with chalcopyrite (Figure 4H). The molybdenite was magnetically separated and then handpicked under a binocular microscope at the Langfang Regional Geological Survey. Fresh, nonoxidized molybdenite powders (<0.1 mm in size and purity >99%) were used for Re–Os isotope analyses. ^{187}Re and ^{187}Os concentrations of molybdenite were measured using a TJA PQ ExCell ICP–MS at the Re–Os Laboratory of National Research Center of Geoanalysis, Chinese Academy of Geological Sciences, Beijing. The chemical separation of the Re and Os and the analytical procedure were in accordance with [18]. The weighed molybdenite samples were loaded into a Carius tube through a thin-neck long funnel. The mixed ^{190}Os and ^{185}Re spike solutions and 2 mL HCl and 4 mL HNO_4 were loaded, while the bottom part of the tube was frozen at $-50\text{ }^\circ\text{C}$ to $-80\text{ }^\circ\text{C}$ in an ethanol–liquid nitrogen slush, and the top was sealed using an oxygen–propane torch. The tube was then placed in a stainless-steel jacket and heated for 24 h at $230\text{ }^\circ\text{C}$. After 24 h and upon cooling, the sample-bearing tubes were opened to transfer the supernatants out and the Os was separated using the method of direct distillation from the Carius tube for 50 min and trapped in 2 mL of water that was used for the ICP–MS (X-Series) determination of the Os isotope ratio. After that, the residual Re-bearing solution was saved in a 150 mL Teflon beaker for Re separation. The residual Re-bearing solution was heated to near-dryness. The acetone phase was transferred to a 150 mL Teflon beaker that contained 1 mL of water. Finally, the solution was picked up in 2% HNO_3 , which was used for the ICP–MS(X-Series) determination of the Re isotope ratio.

The average blanks for the method were ca. 3 pg Re and ca. 0.5 pg Os. The working conditions of the instrument were controlled by the reference material JDC, which produced a measured value of 139.8 ± 2.0 Ma, which is consistent with the recommended value of 139.6 ± 3.8 Ma [41]. The analytical uncertainty in the Re–Os model ages includes 1.02% uncertainty (at 95% confidence level) for the ^{187}Re decay constant. The Re–Os model ages were calculated following the equation: $t = [\ln(1 + ^{187}\text{Os}/^{187}\text{Re})]/\lambda$, where λ is the decay constant of ^{187}Re ($\lambda ^{187}\text{Re} = 1.666 \times 10^{-11}$ year $^{-1}$; [41]) and denotes the age. The Re–Os isochron ages were calculated using the least-squares method [42], employing the program ISOPLOT 3.0 [23].

4. Results

4.1. Zircon U–Pb Dating and Zircon Trace Elements

The Yuhaixi monzonitic granite sample (YHX-ZK-1), diorite sample (ZK001-412), and granite sample (721-6) were selected for LA–ICP–MS zircon U–Pb dating, and the analytical data are listed in Table 1. Most of the zircon grains are euhedral–subhedral and show prismatic forms (100–200 μm long) with aspect ratios of 3:1 to 3:2 and characterized by clear oscillatory growth zoning in the CL images (Figure 5). All samples have varying

U(58–453 ppm) and Th (30–417 ppm) contents with high Th/U ratios (>0.3), which is consistent with a magmatic origin [21].

Table 1. Whole-rock geochemical data of the studied intrusive rocks in the Yuhaixi Mo(Cu) deposit (major elements: wt.%; trace elements: ppm).

Rock Type	Monzonitic Granite			Diorite			Granite		
Sample No.	YHX-ZK-1	YHX-ZK-2	YHX-ZK-3	ZK001-25	ZK001-350	ZK001-396	721-1	721-3	721-5
SiO ₂	74.2	76.57	74.64	53.55	54.58	54.16	74.16	73.79	73.75
TiO ₂	0.17	0.18	0.14	0.95	0.94	0.8	0.2	0.18	0.18
Al ₂ O ₃	13.57	12.42	12.9	17.98	17.33	17.59	13.77	14.15	14.17
TFe ₂ O ₃	1.23	1.31	1	8.69	8.37	7.9	1.49	1.4	1.39
MnO	0.03	0.06	0.03	0.17	0.16	0.14	0.08	0.06	0.06
MgO	0.28	0.36	0.23	4.06	4.84	5.06	0.45	0.39	0.39
CaO	1.23	1.12	1.9	7.97	7.8	7.61	1.65	1.63	1.64
Na ₂ O	3.33	3.39	2.77	3.86	4.11	4.11	4.46	4.57	4.55
K ₂ O	4.97	3.75	4.53	1.15	0.9	1.14	2.65	2.7	2.81
P ₂ O ₅	0.04	0.05	0.04	0.24	0.16	0.25	0.07	0.07	0.07
LOI	0.63	0.73	1.82	1.12	0.8	1.02	0.5	0.47	0.5
TOTAL	99.68	99.94	99.98	99.74	99.99	99.77	99.48	99.41	99.52
Na ₂ O + K ₂ O	8.3	7.14	7.29	5.01	5.01	5.25	7.11	7.28	7.37
Mg [#]	28.87	32.88	29.08	45.44	50.76	53.31	35	33.18	33.34
A/CNK	1.04	1.05	1.06	0.81	0.79	0.81	1.04	1.05	1.05
A/NK	1.25	1.2	1.29	2.37	2.24	2.2	1.35	1.35	1.27
Li	5.44	6.67	1.31	8.67	10.66	8.71	13.79	16.67	12.95
Be	0.89	2.39	0.94	0.97	1.02	0.96	1.05	1.52	1.04
Sc	2.15	3.53	1.14	19.92	24.87	23.37	1.38	2.6	1.38
V	10.66	12.16	9.27	201.07	241.97	116.9	8.35	8.39	7.22
Cr	19.13	0.78	10.53	22.33	67.75	129.44	5.68	8.87	4.1
Co	1.97	1.01	0.56	22.83	30.73	29.04	1.01	1.03	0.88
Ni	0.11	0.73	0.86	18.48	46.27	81.17	0.26	1.81	1.52
Cu	114.22	37.2	10.2	65.43	132.91	55.89	2.01	1.23	2.88
Zn	15.83	74.89	27.69	103.43	102.49	105.55	68.29	44.17	49.97
Ga	14.88	15.67	11.72	22.98	23.43	24.02	15.15	16.25	15.12
Rb	64.57	75.8	64.65	25.2	17.69	25.25	45.6	62.97	45.83
Sr	188.36	168.2	137.76	833.76	784.8	940.51	379.1	400.17	371.33
Y	7.83	14.27	5.77	28.58	25.65	24.64	19.57	18.59	19.64
Zr	94.78	114.16	89.03	364.46	160.19	23.13	120.58	110.57	114.79
Nb	5.35	12.47	5.34	4.52	5.26	4.15	5.4	6.28	4.93
Cs	0.24	0.4	0.4	0.51	0.5	0.57	0.39	1.39	0.38
Ba	853	592	598	369	314	436	1248	1277	1333
La	27.76	27.03	17.31	18.18	19.09	15.35	20.76	35.15	27.57
Ce	51.7	59	38.94	45.57	47.45	41.31	45.29	68.09	53.25
Pr	5.86	6.19	3.93	6.63	6.78	6.23	4.71	8.11	6.57
Nd	21.54	22.74	14.66	30.25	30.26	28.08	18.11	30.56	25.29
Sm	3.39	4.1	2.56	6.66	6.09	5.78	3.35	5.4	4.51
Eu	1.15	0.86	0.82	1.91	1.57	1.58	1.4	1.54	1.51
Gd	2.94	3.4	2.14	5.46	5.05	4.69	2.99	4.43	3.96
Tb	0.36	0.49	0.27	0.9	0.83	0.79	0.49	0.64	0.6
Dy	1.64	2.58	1.16	5.67	4.84	4.65	2.98	3.42	3.47
Ho	0.3	0.52	0.22	1.2	0.99	0.94	0.67	0.67	0.71
Er	0.81	1.43	0.6	3.3	2.77	2.57	1.97	1.87	1.97
Tm	0.11	0.22	0.08	0.49	0.41	0.37	0.3	0.28	0.29
Yb	0.67	1.45	0.53	3.12	2.71	2.42	1.99	1.73	1.95
Lu	0.11	0.24	0.08	0.48	0.44	0.39	0.33	0.28	0.32
Hf	2.77	3.64	2.5	8.98	4.93	1.27	3.67	3.46	3.54

Table 1. Cont.

Rock Type	Monzonitic Granite				Diorite			Granite		
Sample No.	YHX-ZK-1	YHX-ZK-2	YHX-ZK-3	ZK001-25	ZK001-350	ZK001-396	721-1	721-3	721-5	
Ta	0.3	1.34	0.29	0.32	0.34	0.25	0.31	0.48	0.3	
Tl	0.21	0.24	0.19	0.09	0.06	0.08	0.18	0.2	0.16	
Pb	15.31	11.3	11.69	6.2	5.45	8.02	8.42	9.44	8.78	
Bi	0.05	0.03	0.03	0.12	0.1	0.26	0.02	0.04	0.02	
Th	5.77	8.18	5.8	3.06	3.35	1.18	5.21	9.97	7.37	
U	1.13	1.95	0.99	2.19	1.46	0.83	1.19	1.82	1.46	
(La/Yb) _N	27.9	12.55	21.98	3.92	4.74	4.28	7.02	13.71	9.54	
(Tb/Yb) _N	2.37	1.5	2.24	1.29	1.36	1.45	1.1	1.63	1.36	
(La/Sm) _N	5.15	4.15	4.26	1.72	1.97	1.67	3.9	4.09	3.84	
Th/Ce	0.11	0.14	0.15	0.07	0.07	0.03	0.12	0.15	0.14	
Th/U	5.12	4.2	5.84	1.4	2.29	1.42	4.39	5.48	5.05	
Ce/Pb	3.38	5.22	3.33	7.35	8.7	5.15	5.38	7.22	6.06	
ΣREE	118.34	130.24	83.29	129.82	129.29	115.14	105.33	162.16	131.97	
Eu	1.09	0.68	1.05	0.94	0.84	0.9	1.33	0.94	1.07	
Sr/Y	24.05	11.78	23.88	29.17	30.59	38.17	19.38	21.53	18.91	

Note: $Mg^{\#} = 100 \times (MgO/40.3044)/(MgO/40.3044 + 0.8998 \times Fe_2O_3^T/71.8440)$.

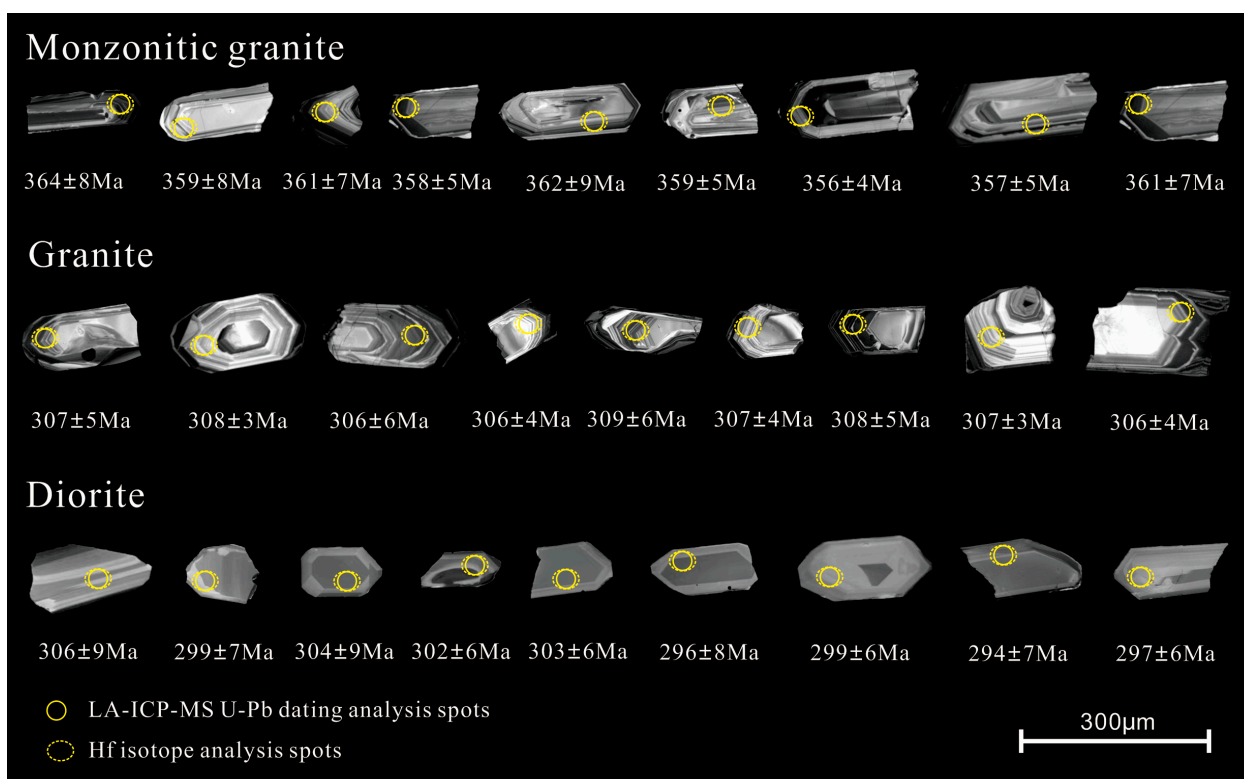


Figure 5. Cathodoluminescence images of representative zircon grains of the Yuhaixi showing the inner structures and analyzed spots.

Except for two discordant spot (02, 05), the remaining 17 analyses from the monzonitic granite sample (YHX-ZK-1) yielded concordant ²⁰⁶Pb/²³⁸U ages varying from 352 to 362 Ma (Figure 6), with a weighted mean age of 359.4 ± 1.6 Ma (MSWD = 0.89), which is interpreted as the best estimate of emplacement age for the Yuhaixi monzonitic granite.

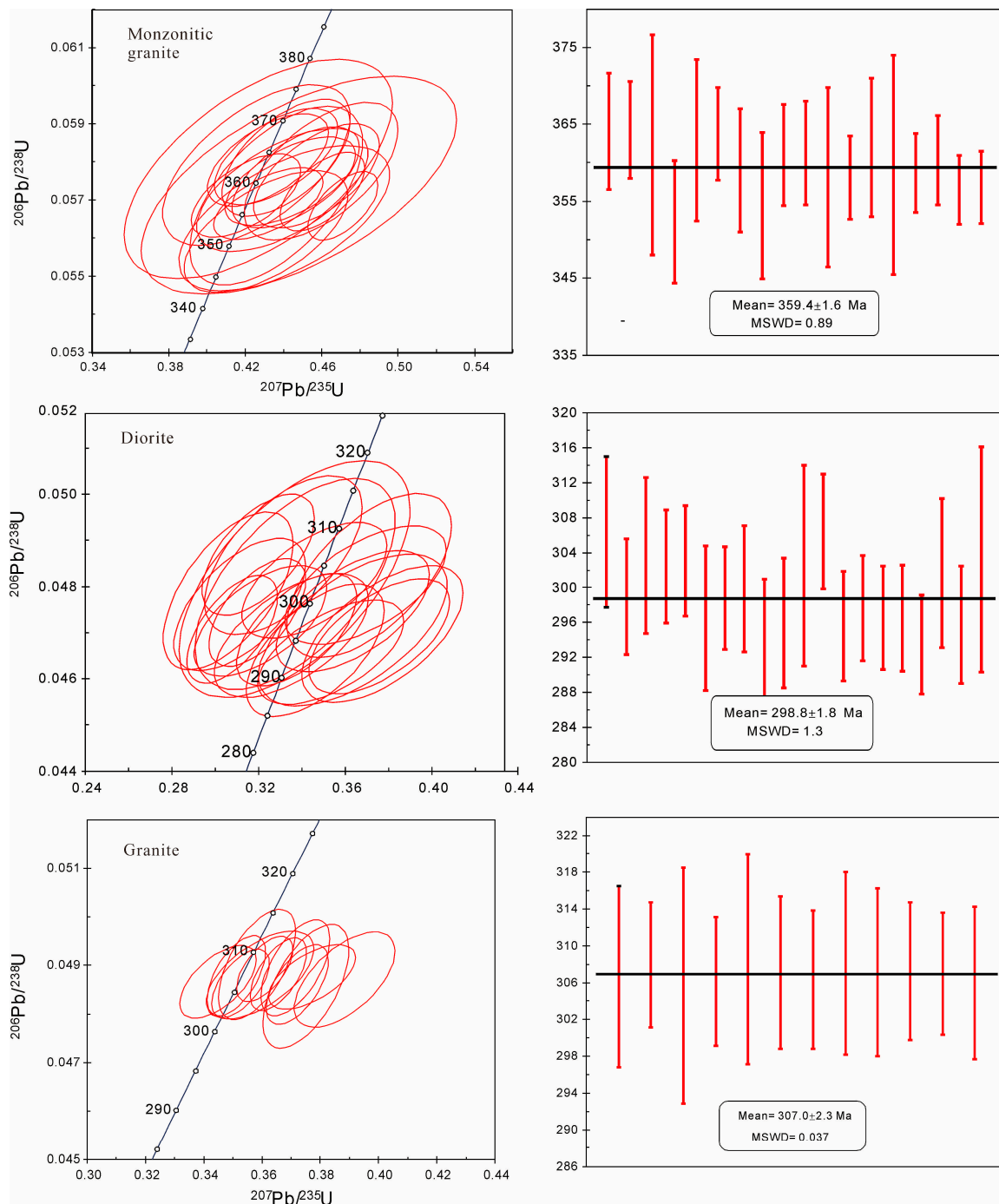


Figure 6. U-Pb concordia diagrams and weighted average ages of the zircons from monzonitic granite, diorite, and granite in the Yuhaxi porphyry Mo(Cu) deposit.

Except for three discordant spots (07, 09, 11), the remaining 12 analytical spots from the granite sample (721-6) had $^{206}\text{Pb}/^{238}\text{U}$ ages ranging from 306 to 309 Ma (Figure 6), with a weighted mean age of 307.0 ± 2.3 Ma (MSWD = 0.037).

Except for three discordant spots (03, 07 and 16), the remaining 19 analytical spots from the diorite sample (ZK001-412) had $^{206}\text{Pb}/^{238}\text{U}$ ages ranging from 296 to 306 Ma. (Figure 6), with a weighted mean age of 298.8 ± 1.8 Ma (MSWD = 1.3) (Table 2).

Table 2. Cont.

Spot	Element ($\times 10^{-6}$)			Isotope Ratio						Apparent Age (Ma)					
	Pb	Th	U	$^{207}\text{Pb}/^{206}\text{Pb}$	1σ	$^{207}\text{Pb}/^{235}\text{U}$	1σ	$^{206}\text{Pb}/^{238}\text{U}$	1σ	$^{207}\text{Pb}/^{206}\text{Pb}$	1σ	$^{207}\text{Pb}/^{235}\text{U}$	1σ	$^{206}\text{Pb}/^{238}\text{U}$	1σ
zk001-14	9	86	127	0.0489	0.0045	0.3209	0.025	0.0473	0.001	143	200	283	19	298	6
zk001-15	6	57	84	0.0485	0.0038	0.3079	0.017	0.0471	0.001	124	174	273	13	297	6
zk001-16	8	90	117	0.0505	0.0037	0.3377	0.0227	0.0471	0.001	217	177	295	17	296	6
zk001-17	6	46	101	0.0554	0.0049	0.3534	0.0275	0.0466	0.0009	428	198	307	21	293	6
zk001-18	11	102	153	0.0461	0.004	0.3058	0.0245	0.0479	0.0014	400	-202	271	19	302	9
zk001-19	5	41	83	0.053	0.0054	0.3352	0.029	0.0469	0.0011	328	230	294	22	296	7
zk001-20	4	36	67	0.0533	0.0082	0.3365	0.0437	0.0482	0.0021	343	315	295	33	303	13
Granite															
721-6-01	6	106	87	0.0584	0.0021	0.3884	0.0141	0.0487	0.0008	546	84	333	10	307	5
721-6-02	26	475	350	0.0534	0.001	0.3608	0.0079	0.0489	0.0005	346	44	313	6	308	3
721-6-03	30	369	453	0.0559	0.0014	0.3752	0.012	0.0486	0.001	456	56	323	9	306	6
721-6-05	20	177	327	0.0525	0.001	0.3526	0.008	0.0486	0.0006	306	46	307	6	306	4
721-6-07	16	131	258	0.0529	0.0012	0.3582	0.0108	0.049	0.0009	324	52	311	8	309	6
721-6-08	16	248	216	0.0522	0.0011	0.3511	0.0082	0.0488	0.0007	295	50	306	6	307	4
721-6-11	17	198	269	0.0513	0.0015	0.3449	0.0108	0.0487	0.0006	254	67	301	8	306	4
721-6-13	12	178	170	0.0553	0.0014	0.3714	0.0096	0.0489	0.0008	433	57	321	7	308	5
721-6-16	5	63	62	0.0536	0.0023	0.3594	0.0151	0.0488	0.0007	367	96	312	11	307	5
721-6-21	21	204	338	0.0542	0.001	0.3656	0.0078	0.0488	0.0006	376	38	316	6	307	4
721-6-22	12	193	162	0.0559	0.0017	0.3772	0.0122	0.0488	0.0005	450	64	325	9	307	3
721-6-23	33	417	478	0.0553	0.0012	0.3721	0.0087	0.0486	0.0007	433	51	321	6	306	4

The calculated results of zircon Ce^{4+}/Ce^{3+} and Ti-in-zircon thermometer have been used to estimate the magma temperatures and oxidation states [17], with the detailed calculation procedures being presented by [17]. In this study, the zircon Ce^{4+}/Ce^{3+} values of the monzonitic granite, diorite, and granite were calculated to be ~6–248 (avg. 60), 11–182 (avg. 54), and 6–241 (avg. 85), respectively (Table 3). Ti-in-zircon temperatures were calculated to be 590–954 °C (avg. 744 °C) for the monzonitic granite, 698–775 °C (avg. 728 °C), for the diorite and 653–917 °C (avg. 712 °C) for the granite (Table 3). The zircon REE patterns are commonly featured by HREE enrichments with positive Ce anomalies and negative Eu anomalies (Figure 7).

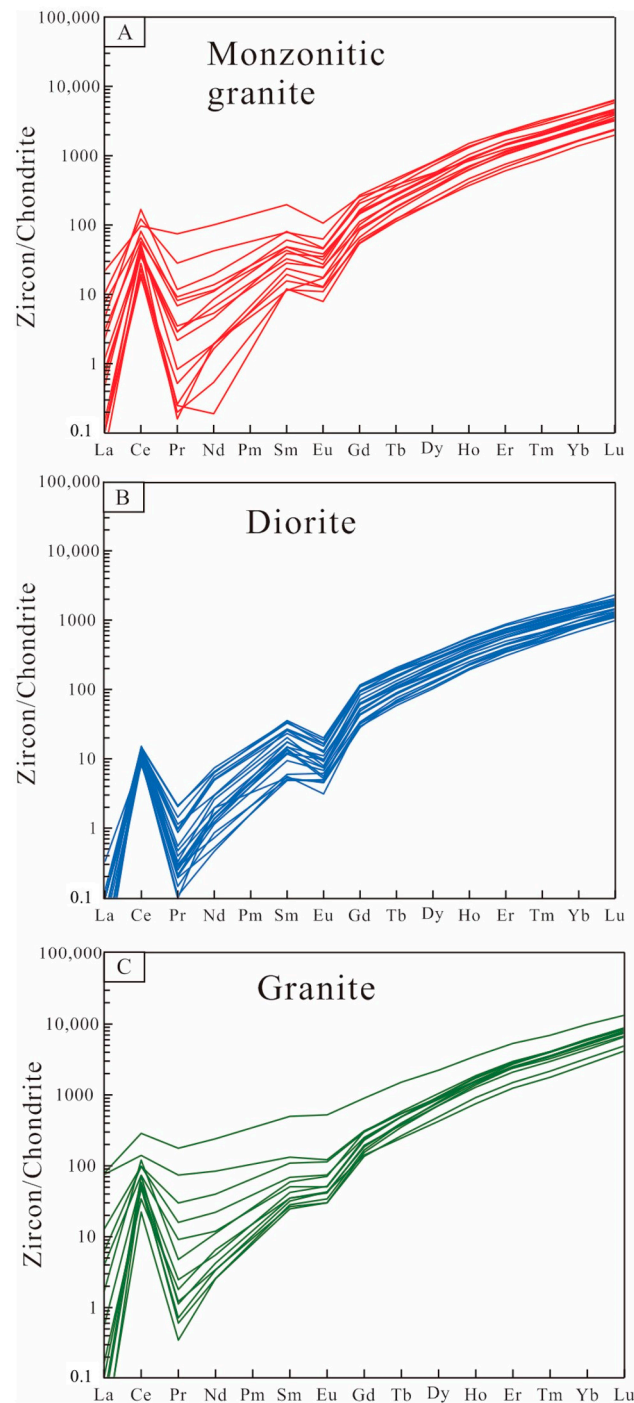


Figure 7. Chondrite-normalized REE patterns for zircon grains from the Yuhai intrusions. Chondrite values are from [20].

Table 3. Trace element abundance (in ppm), Eu anomalies, and Ce⁴⁺/Ce³⁺ in zircon and Ti-in-zircon temperature.

Analysis	Ti	Y	La	Ce	Pr	Nd	Sm	Eu	Gd	Tb	Dy	Ho	Er	Tm	Yb	Lu	Eu/Eu*	T
YHX-ZK-1	38	1860	9.55	101	11	63.5	34.9	7.57	63	15.5	154	56.7	257	55	525	114	0.52	732
YHX-ZK-2	8.1	3041	3.15	99.1	3.4	25.5	15.3	4.62	70	22.1	261	108	466	105	918	200	0.56	745
YHX-ZK-3	5.2	2093	0.04	32.2	0.3	2.73	7.59	2.57	39	12.6	159	65.3	298	64.9	606	130	0.45	747
YHX-ZK-4	5.9	1501	0.2	33.4	0.4	3.21	5.53	1.82	23	8.64	112	49.2	245	54.7	521	125	0.41	748
YHX-ZK-5	27	3836	12.5	137	15	88.1	57.1	11.1	118	33.3	356	138	601	128	1137	252	0.49	677
YHX-ZK-6	6.1	1496	0.35	32.9	0.4	3.96	6.36	1.77	29	10.4	128	50.8	236	52.5	526	108	0.47	715
YHX-ZK-7	6.2	1879	0.24	28.6	0.4	5.12	9.43	2.32	41	13.2	167	64	299	63.8	597	135	0.35	631
YHX-ZK-8	13	2846	1.38	136	1.4	11.6	15.8	3.42	59	20.4	257	97.9	431	90.9	824	187	0.37	815
YHX-ZK-9	12	2797	0.69	65.9	1	6.91	8.41	2	43	17.2	232	94.2	452	97.8	925	206	0.41	745
YHX-ZK-10	6	1867	0.14	43	0.1	1.15	4.61	1.29	26	11	138	62.7	310	68.3	629	148	0.36	637
YHX-ZK-11	17	2089	2.31	53.1	0.8	6.62	11.9	3.34	53	15.7	175	74.6	350	72.1	694	151	0.70	731
YHX-ZK-12	1.6	1329	0.02	22.7	0	0.98	3.79	0.95	22	8.39	111	44.5	223	50.2	473	103	0.52	884
YHX-ZK-13	22	2186	0.92	46.7	1.1	8.24	9.48	2.81	38	12.9	160	65.9	305	68.2	674	140	0.42	955
YHX-ZK-14	24	1112	0.54	28.1	0.2	2.7	3.87	1.32	22	6.98	98	40.1	178	38.9	357	83	0.48	693
YHX-ZK-15	17	5436	17.6	178	20	124	76.3	16.8	177	49.1	527	185	800	168	1441	298	0.41	692
YHX-ZK-16	3.3	2710	0.51	38	0.7	7.62	11.2	3.02	58	19.3	227	85.2	377	81.3	747	159	0.64	626
zk001-412-1	9.1	956	0.02	9.89	0.1	3.49	5.43	1.25	26	7.73	87	31.7	146	30.8	277	57	0.47	799
zk001-412-2	8.4	515	0.11	8.09	0	1.22	1.07	0.34	7.6	3.4	41	16.8	76.2	18.7	182	38	0.43	741
zk001-412-3	6.2	820	0.01	12.3	0	0.85	2.37	0.57	17	5.93	69	27.9	124	27.9	259	54	0.40	799
zk001-412-4	6.7	907	0.01	11.5	0.1	1.83	4.09	0.6	19	6.5	78	30.1	132	29.2	275	60	0.35	787
zk001-412-5	5.9	809	0.04	12.1	0	0.75	2.68	0.4	13	5.12	66	25.9	123	26.4	256	56	0.40	778
zk001-412-6	8.8	574	0.01	10.1	0	0.71	1.9	0.52	12	4.17	51	18.8	85.9	18.9	177	37	0.30	749
zk001-412-7	9.4	446	0.01	7.37	0	0.53	1.01	0.36	7.9	2.86	34	14.3	66.8	15.7	149	33	0.30	782
zk001-412-8	9.8	658	0.01	7.69	0	1.61	3.52	0.74	16	5.21	58	21.9	96.2	20.4	189	39	0.23	757
zk001-412-9	8.7	1111	0	12.1	0.3	4.6	6.9	1.26	31	9.23	101	36.7	163	34.3	308	63	0.22	745
zk001-412-10	14	1237	0.01	11.2	0.2	3.91	7.2	1.52	31	10.1	112	40.9	182	37.6	336	69	0.37	783
zk001-412-11	8.6	649	0.01	8.97	0	0.98	2.79	0.43	12	4.38	52	21.5	98.7	22.1	216	48	0.42	790
zk001-412-12	11	1265	0	12.5	0.3	4.06	6.62	1.42	31	9.51	110	42	191	41.8	354	77	0.32	794
zk001-412-13	5.8	552	0.01	8.09	0	0.29	1.13	0.24	9.1	3.27	42	17.5	82.8	19.2	189	41	0.28	766
zk001-412-14	6.7	1109	0.02	11.7	0.1	3.15	5.28	1.16	29	8.81	103	37.7	161	36	324	65	0.26	766
7216-1	6.4	1636	0.05	26.9	0.2	3.83	6.68	3.07	36	11.3	134	52.8	256	56.2	555	131	0.55	752
7216-2	9.3	3942	0.51	95	0.6	6.55	11.3	5.1	77	26.8	330	131	610	129	1234	276	0.48	789
7216-3	6.3	3785	1.19	58.2	1.1	7.02	9.66	3.63	58	22.6	299	125	600	130	1255	272	0.46	733
7216-4	5.3	3706	0.16	46.2	0.3	3.23	8.03	3.7	61	22.6	297	121	577	127	1200	265	0.45	739
7216-5	5.6	3438	0	43.7	0.1	1.51	5.39	2.45	42	18	253	111	558	127	1250	279	0.44	666
7216-6	2.4	3024	0	17.6	0	1.5	4.7	2.16	39	16.2	224	97.3	495	112	1110	252	0.45	776
7216-7	8.2	2765	0.02	57	0.1	2.48	6.69	2.97	49	17.3	223	90.1	431	94.1	890	208	0.50	771
7216-8	9.4	3352	1.86	77.4	1.9	13	13.1	5.35	64	22.6	273	109	517	113	1072	241	0.45	747
7216-9	11	3309	3.84	77.9	3.6	23.4	20.8	8.18	76	25	285	109	489	103	973	215	0.56	772
7216-10	48	7715	23.6	227	21	141	95.1	37.6	228	69.6	704	248	1096	220	2021	419	0.63	695
7216-11	6.1	1957	0.02	42	0.2	2.01	5.07	2.16	35	12.2	155	64.5	308	68.6	672	156	0.57	742
7216-12	11	3451	22.8	111	8.8	49.4	25.3	8.75	79	25.3	291	111	506	110	1044	235	0.49	712
7216-13	7.9	1906	0.08	37.7	0.2	2.07	5.13	2.62	33	11.5	148	62.1	301	69.1	693	158	0.51	730
7216-14	3.4	720	0	11.6	0.1	1.63	2.86	1.43	14	4.39	55	22.6	113	27	300	77	0.46	753
7216-15	5.8	1816	0.02	34.9	0.1	1.93	4.62	2.52	32	11.4	143	59.5	281	64	620	144	0.48	731

¹ (Eu/Eu*) = Eu/(Sm × Gd)^{1/2} [18]. ² Ti-in-zircon temperatures are calculated using the equation proposed by [22]: log (ppm Ti-in-zircon) = (5.711 ± 0.072) − (4800 ± 86)/T(K) − log αSiO₂ + log αTiO₂, where αSiO₂ = 1, αTiO₂ = 0.6 are used in the calculation.

4.2. Whole-Rock Major and Trace Elements

The representative whole-rock geochemical data for the Yuhaxi intrusive samples are presented in Table 1. The Yuhaxi monzonitic granite, granite and diorite samples plot inside the granite, granite and monzodiorite fields, respectively on the Na₂O + K₂O vs. SiO₂ diagram (Figure 8a; [37]). The Yuhaxi monzonitic granites are characterized by high SiO₂ (74.20–76.57 wt.%) and total alkali contents (K₂O + Na₂O = 7.14–8.30 wt.%), but low MgO (0.23–0.36 wt.%), TiO₂ (0.14–0.17 wt.%), and P₂O₅ (0.04–0.05 wt.%), with low Mg[#] = 28–32 [100 × molecular Mg²⁺/(Mg²⁺ + Fe²⁺)], which belong to the high-K calc-alkaline series (Figure 8b). The Yuhaxi post-ore granite exhibited similar major element compositions, but they show relatively high Na₂O and low K₂O contents relative to the monzonitic granites. These rocks are characterized by high SiO₂ and K₂O + Na₂O (7.11–7.37 wt.%) contents, which suggests that they are high-K calc-alkaline series rocks (Figure 8b). The Yuhaxi diorite is chemically different from the Yuhaxi monzonitic granite and granite,

and has SiO_2 , Al_2O_3 , Na_2O , K_2O , TFe_2O_3 , TiO_2 , and P_2O_5 contents of 53.55–54.58 wt.%, 17.33–17.98 wt.%, 3.86–4.11 wt.%, 0.90–1.15 wt.%, 7.90–8.69 wt.%, 0.80–0.95 wt.%, and 0.16–0.25 wt.%, respectively. The Yuhaxi diorite belongs to the calc-alkaline series (Figure 8b). In the A/NK vs. A/CNK diagram, the Yuhaxi monzonitic granite and granite samples are metaluminous to weak peraluminous (Figure 8c), with an aluminum saturation index ($\text{Al}_2\text{O}_3/(\text{Na}_2\text{O} + \text{K}_2\text{O} + \text{CaO})$) ranging from 0.66–1.07.

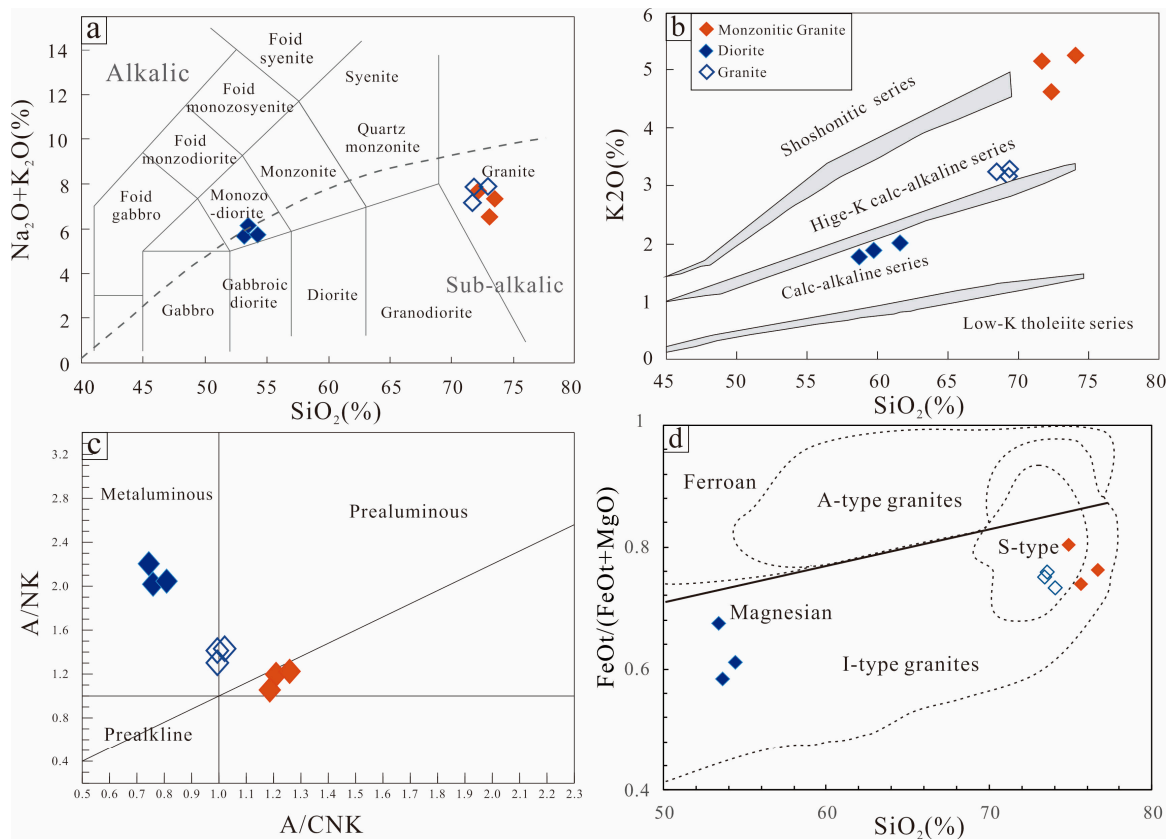


Figure 8. Classification and series diagrams of intrusions in the Yuhaxi porphyry Mo(Cu) deposit. (a) $\text{Na}_2\text{O} + \text{K}_2\text{O}$ vs. SiO_2 plot diagram [43]. (b) K_2O vs. SiO_2 diagram [44]. (c) A/NK vs. A/CNK plot diagram [45]. (d) $\text{FeOt}/(\text{FeO} + \text{MgO})$ vs. SiO_2 diagram.

As for the chondrite-normalized REE patterns, the Yuhaxi diorite samples are moderately fractionated ($(\text{La}/\text{Yb})_N = 4.19\text{--}7.64$), with light rare earth element (LREE) enrichment and heavy rare earth element (HREE) depletion in the absence of clear Eu anomalies ($\text{Eu}/\text{Eu}^* = 0.92\text{--}1.27$) (Figure 9A). The overall rare earth content is low ($\Sigma\text{REE} = 32.1\text{--}162.16$) in Yuhaxi, among which the rare earth content of granite is the lowest ($\Sigma\text{REE} = 32.1\text{--}78.49$). The granite samples show a slight positive Eu anomaly ($\delta\text{Eu} = 0.94\text{--}1.33$). The diorite samples show weaker negative Eu anomalies ($\delta\text{Eu} = 0.84\text{--}0.94$) (Figure 9A). In the primitive mantle-normalized trace element spider diagram (Figure 9A; [30]), different magmatic rocks show different characteristics, which are generally characterized by enrichment of large-ion lithophile elements (LILE: Rb, Ba, K, U) and relative depletion of high-field-strength elements (HFSE: Nb, Ta, Zr). The monzonite granite is enriched in Rb, Ba, U, K, Pb, and depleted of Nb, Ta, Sr, Ti, P. Compared with granite, the LILE enrichment and the HFSE depletion in monzonitic granite and diorite are more significant (Figure 9A).

4.3. Zircon Hf Isotopes

Zircon Hf isotope analysis results are listed in Table 4. The monzonitic granite, diorite, and granite yielded $\epsilon\text{Hf}(t)$ values of 11.37–17.59, 11.59–13.46, and 11.73–14.76, respectively. The zircon Hf single- and two-stage model ages are 280–538 Ma and 240–637 Ma for the

monzonitic granite, 399–472 Ma and 458–578 Ma for the diorite, and 354–478 Ma and 377–572 Ma for the granite, respectively (Table 4).

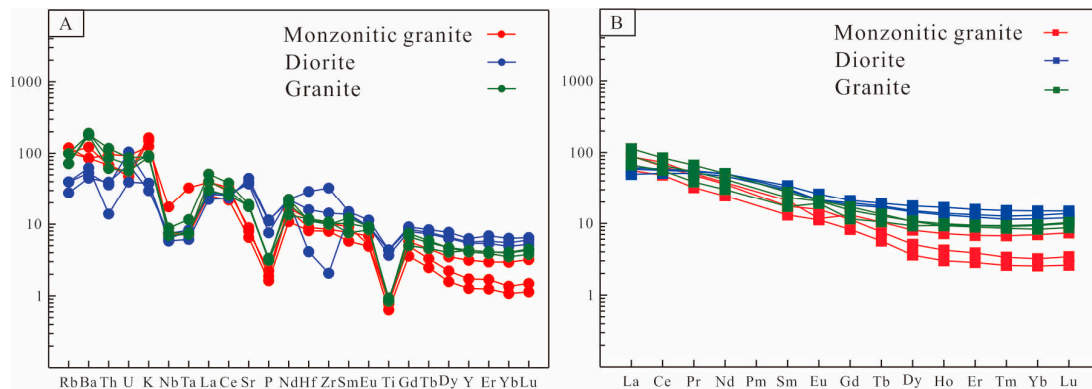


Figure 9. (A) primitive mantle-normalized trace element abundance spider diagram and (B) chondrite-normalized REE of the intrusions in the Yuhaixi porphyry Mo(Cu) deposit. (normalization values are from [20]). The N-MORB, E-MORB, and OIB patterns are from [20].

4.4. Whole-Rock Sr-Nd Isotopes

The initial $^{87}\text{Sr}/^{86}\text{Sr}$ (i) isotope ratios and $\epsilon\text{Nd}(t)$ were calculated using the $^{87}\text{Sr}/^{86}\text{Sr}$ ratios, Nd values, and zircon U-Pb ages analyzed in this study (Table 5). All rock samples from the Yuhaixi Mo(Cu) deposit (e.g., monzonitic granite, diorite and granite) are characterized by low $(^{87}\text{Sr}/^{86}\text{Sr})_i$ values with obviously varied ranges (e.g., 0.7043–0.7128, 0.7037–0.7041, and 0.7042–0.7043, respectively). They show positive and narrow ranges of $\epsilon\text{Nd}(t)$ (1.36–3.4, 5.16–7.75, and 4.62–6.44, respectively), corresponding to $T_{\text{DM}2}$ ages of 832–1002 Ma, 430–642 Ma, and 545–693 Ma, respectively (Table 5).

4.5. Re-Os Isotopic Ages

The Re-Os isotopic data for nine molybdenite samples from the Yuhaixi porphyry Mo deposit are listed in Table 6 and are plotted in an isochron diagram in Figure 10. The concentrations of ^{187}Re and ^{187}Os ranged from 93.9 to 322.9 $\mu\text{g/g}$ and from 539.5 to 1889.2 ng/g, respectively. Nine samples yielded model ages ranging from 337.9 ± 6.7 to 350.2 ± 6.1 Ma and a well-constrained ^{187}Re – ^{187}Os isochron age of 354.1 ± 6.8 Ma, with $\text{MSWD} = 1.7$ and an initial ^{187}Os of 24 ± 17 ng/g (Figure 10A). The data also yields a weighted average age of 344.5 ± 3.1 Ma ($\text{MSWD} = 2.1$) (Figure 10B). These ages are concordant within the errors, indicating that the Yuhaixi Mo(Cu) deposit was formed in the Carboniferous.

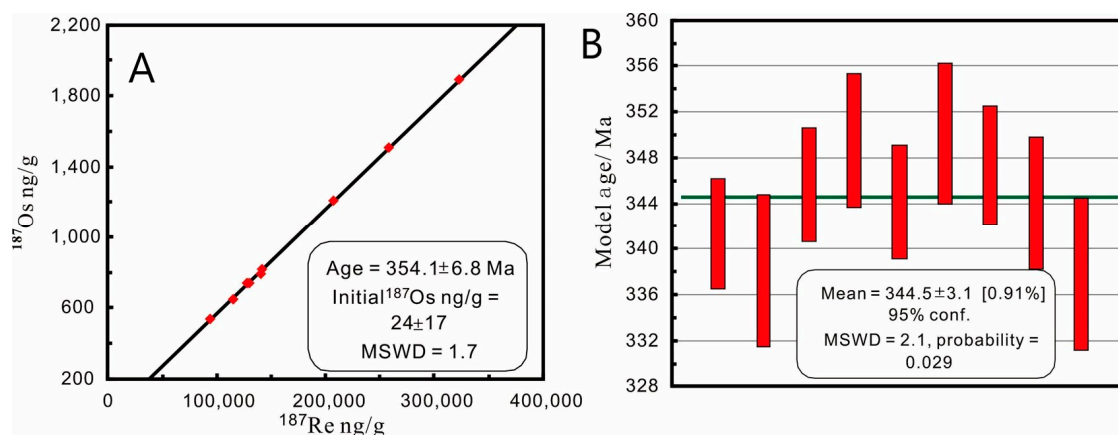


Figure 10. Re-Os isochron diagram and weighted average model age diagram for four molybdenite samples in the Yuhaixi porphyry Mo(Cu) deposit.

Table 4. In situ zircon Hf isotopic data on the studied intrusive rocks in the Yuhaixi Mo(Cu) deposit.

Sample No.	Age (Ma)	$^{176}\text{Hf}/^{177}\text{Hf}$	1 σ	$^{176}\text{Lu}/^{177}\text{Hf}$	1 σ	$^{176}\text{Yb}/^{177}\text{Hf}$	1 σ	eHf (0)	eHf (T)	T _{DM}	T _{DMC}	fs
Monzonitic granite												
YHX-ZK-1	364.07	0.283072	0.000014	0.004346	0.000038	0.125695	0.000845	10.61	17.59	279.05	240.34	−0.87
YHX-ZK-2	364.28	0.282921	0.000016	0.002443	0.000049	0.068981	0.001428	5.27	12.71	487.64	553.83	−0.93
YHX-ZK-3	362.36	0.282939	0.000013	0.002261	0.000021	0.062658	0.00063	5.91	13.34	458.91	511.47	−0.93
YHX-ZK-4	352.34	0.282972	0.000017	0.002645	0.000092	0.076706	0.002935	7.09	14.23	414.25	446.94	−0.92
YHX-ZK-5	362.89	0.282947	0.000014	0.001811	0.000013	0.051511	0.000516	6.18	13.74	442.01	486.6	−0.95
YHX-ZK-6	363.7	0.282929	0.000015	0.002913	0.000044	0.085132	0.001176	5.56	12.87	481.81	542.82	−0.91
YHX-ZK-7	358.97	0.282965	0.000014	0.001719	0.000046	0.048263	0.001292	6.83	14.32	414.48	445.98	−0.95
YHX-ZK-8	354.4	0.282978	0.000016	0.003775	0.000091	0.106083	0.002773	7.3	14.22	418.43	449.15	−0.89
YHX-ZK-9	361	0.282947	0.000013	0.001313	0.000006	0.035821	0.000127	6.21	13.84	435.14	478.51	−0.96
YHX-ZK-10	361.26	0.282985	0.000016	0.003241	0.000026	0.088301	0.000827	7.54	14.72	401.89	422.3	−0.9
YHX-ZK-11	358.08	0.282945	0.000016	0.002979	0.000054	0.083992	0.001507	6.12	13.3	459.23	511.2	−0.91
YHX-ZK-12	358.06	0.282903	0.000013	0.002089	0.000038	0.056193	0.001068	4.62	12.01	509.8	593.52	−0.94
YHX-ZK-13	361.99	0.28288	0.000014	0.001761	0.000034	0.046745	0.000888	3.82	11.37	538.24	637.96	−0.95
YHX-ZK-14	359.72	0.282956	0.000014	0.001655	0.000009	0.046342	0.000231	6.52	14.05	426.25	464.2	−0.95
YHX-ZK-15	358.69	0.282968	0.000016	0.003117	0.000047	0.087435	0.001308	6.93	14.08	426.66	461.17	−0.91
YHX-ZK-16	360.35	0.282957	0.000016	0.001848	0.000006	0.048001	0.000285	6.53	14.03	427.98	466	−0.94
YHX-ZK-17	356.41	0.283007	0.000014	0.003289	0.000063	0.097506	0.001856	8.3	15.37	369.99	376.79	−0.9
YHX-ZK-18	356.81	0.282927	0.000018	0.003289	0.000045	0.096394	0.001396	5.49	12.57	490.31	557.13	−0.9
Diorite												
zk001-412-1	306.4	0.282943	0.000014	0.000731	0.00001	0.02065	0.000259	6.04	12.64	434.94	513.32	−0.98
zk001-412-2	298.94	0.282967	0.000014	0.000688	0.000001	0.01916	0.000048	6.9	13.34	400.38	462.42	−0.98
zk001-412-3	303.67	0.282969	0.000016	0.000888	0.000002	0.026311	0.000066	6.95	13.46	400.35	458.66	−0.97
zk001-412-4	302.43	0.282938	0.000016	0.001176	0.000012	0.033611	0.000286	5.87	12.29	447.19	532.71	−0.96
zk001-412-6	303.05	0.282944	0.000012	0.000827	0.000005	0.023606	0.00012	6.09	12.59	434.22	513.67	−0.98
zk001-412-7	296.45	0.282927	0.000012	0.000631	0.000004	0.018343	0.000149	5.5	11.9	455.47	553.11	−0.98
zk001-412-8	298.79	0.282937	0.000014	0.000837	0.000016	0.024897	0.000592	5.85	12.26	443.87	531.68	−0.97
zk001-412-9	299.82	0.282946	0.000014	0.000701	0.000003	0.020066	0.000103	6.16	12.62	430.05	509.63	−0.98
zk001-412-10	293.73	0.282967	0.000011	0.000607	0.000005	0.017496	0.000137	6.91	13.26	398.9	463.59	−0.98
zk001-412-11	295.9	0.282925	0.000013	0.000574	0.000001	0.016515	0.000039	5.41	11.81	458.27	558.37	−0.98
zk001-412-12	302.54	0.282914	0.000015	0.000449	0.000011	0.012607	0.000408	5.02	11.59	472.15	577.62	−0.99
zk001-412-13	306.43	0.28294	0.000013	0.00094	0.000005	0.027755	0.000198	5.95	12.51	440.87	521.65	−0.97
zk001-412-14	295.58	0.282937	0.000012	0.00096	0.000001	0.02861	0.000066	5.83	12.14	446.22	536.6	−0.97
zk001-412-15	297.65	0.282955	0.000012	0.000885	0.000003	0.025982	0.000121	6.48	12.86	419.08	492.32	−0.97
zk001-412-16	296.55	0.282953	0.000013	0.000649	0.000003	0.018522	0.000146	6.41	12.81	419.37	494.69	−0.98
zk001-412-17	296.48	0.282952	0.000014	0.001076	0.000004	0.032282	0.000155	6.38	12.69	425.56	502.38	−0.97
zk001-412-18	293.48	0.282934	0.000013	0.000679	0.000002	0.019199	0.000088	5.73	12.05	446.96	540.9	−0.98
zk001-412-19	301.64	0.282966	0.000017	0.000677	0.000003	0.018615	0.000083	6.87	13.38	401.16	462.08	−0.98
zk001-412-20	295.72	0.282931	0.000011	0.000607	0.000005	0.016322	0.000143	5.62	12.01	450.39	545.54	−0.98
zk001-412-21	303.2	0.282938	0.000015	0.000835	0.000009	0.024164	0.000315	5.87	12.38	442.95	527.54	−0.97

Table 4. Cont.

Sample No.	Age (Ma)	¹⁷⁶ Hf/ ¹⁷⁷ Hf	1σ	¹⁷⁶ Lu/ ¹⁷⁷ Hf	1σ	¹⁷⁶ Yb/ ¹⁷⁷ Hf	1σ	eHf (0)	eHf (T)	T _{DM}	T _{DMC}	fs
Granite												
7216-1	306.63	0.282925	0.000034	0.00212	0.000015	0.052126	0.000742	5.41	11.73	477.66	571.8	−0.94
7216-2	307.95	0.28298	0.000027	0.004211	0.000022	0.108632	0.000672	7.36	13.28	421.22	473.44	−0.87
7216-3	305.7	0.283025	0.000023	0.004513	0.000057	0.114445	0.001314	8.94	14.76	354.81	376.83	−0.86
7216-4	306.15	0.282992	0.000019	0.004137	0.000074	0.106852	0.002601	7.78	13.68	401.84	446.26	−0.88
7216-5	308.54	0.282968	0.000014	0.003326	0.000032	0.088744	0.001145	6.94	13.06	428.42	488.23	−0.9
7216-6	307.07	0.282947	0.000021	0.002676	0.000013	0.07104	0.000482	6.19	12.41	452.27	528.74	−0.92
7216-7	306.32	0.282989	0.000019	0.004237	0.000041	0.110844	0.001475	7.69	13.58	406.88	453.14	−0.87
7216-8	308.07	0.282945	0.000019	0.0022	0.000039	0.05607	0.001128	6.11	12.44	449.83	527.37	−0.93
7216-9	307.16	0.282962	0.00002	0.001427	0.000076	0.033621	0.001796	6.71	13.18	416.07	479.25	−0.96

Note: $\epsilon\text{Hf}(0) = [({}^{176}\text{Hf}/{}^{177}\text{Hf})_s / ({}^{176}\text{Hf}/{}^{177}\text{Hf})_{\text{CHUR},0} - 1] \cdot 10,000$; $\epsilon\text{Hf}(t) = \{ [({}^{176}\text{Hf}/{}^{177}\text{Hf})_s - ({}^{176}\text{Lu}/{}^{177}\text{Hf})_s \cdot (e^{\lambda t} - 1)] / [({}^{176}\text{Hf}/{}^{177}\text{Hf})_{\text{CHUR},0} - ({}^{176}\text{Lu}/{}^{177}\text{Hf})_{\text{CHUR},0} \cdot (e^{\lambda t} - 1)] - 1 \} \cdot 10,000$; $T_{\text{DM1}} = 1/\lambda \cdot \ln\{1 + [({}^{176}\text{Hf}/{}^{177}\text{Hf})_s - ({}^{176}\text{Hf}/{}^{177}\text{Hf})_{\text{DM}}] / [({}^{176}\text{Lu}/{}^{177}\text{Hf})_s - ({}^{176}\text{Lu}/{}^{177}\text{Hf})_{\text{DM}}]\}$; $T_{\text{DM2}} = T_{\text{DM1}} - (T_{\text{DM1}} - t) \cdot (f_{\text{cc}} - f_s) \cdot (f_{\text{cc}} - f_{\text{DM}})$; $f_{\text{Lu}/\text{Hf}} = [({}^{176}\text{Lu}/{}^{177}\text{Hf})_s / ({}^{176}\text{Lu}/{}^{177}\text{Hf})_{\text{CHUR},0}] - 1$, where $({}^{176}\text{Hf}/{}^{177}\text{Hf})_s$ and $({}^{176}\text{Lu}/{}^{177}\text{Hf})_s$ are the measured values of the samples, $s = \text{sample}$, and $t = \text{crystallization time of zircon}$; $({}^{176}\text{Lu}/{}^{177}\text{Hf})_{\text{CHUR},0} = 0.0332$ and $({}^{176}\text{Hf}/{}^{177}\text{Hf})_{\text{CHUR},0} = 0.282772$ [23]; $({}^{176}\text{Lu}/{}^{177}\text{Hf})_{\text{DM}} = 0.0384$ and $({}^{176}\text{Hf}/{}^{177}\text{Hf})_{\text{DM}} = 0.28325$ [24]; $f_{\text{cc}} = -0.55$ and $f_{\text{DM}} = 0.16$; and $\lambda = 1.867 \times 10^{-12} \text{ yr}^{-1}$ [46] were used in the calculation.

Table 5. Sr–Nd isotopic compositions of the studied intrusive rocks in the Yuhaxi Mo(Cu) deposit.

Sample No.	Rock Type	Age (Ma)	Rb	Sr	⁸⁷ Rb/ ⁸⁶ Sr	⁸⁷ Sr/ ⁸⁶ Sr	I _{Sr}	Sm	Nd	¹⁴⁷ Sm/ ¹⁴⁴ Nd	¹⁴³ Nd/ ¹⁴⁴ Nd	Sm/Nd	I _{Nd}	εNd(0)	εNd(t)	T _{DM}
YHX-ZK-1	MG	359.4	30.9563	107	0.8371	0.711	0.7062	4.545	13.95	0.197	0.5127	0.326	0.5122	1.3655	1.3597	3992
YHX-ZK-2	MG	359.4	28.9275	68.65	1.2193	0.711	0.7043	1.948	6.905	0.171	0.5127	0.282	0.5123	1.4045	2.6103	1555
S3201-20	GNG	364	58.6	289	0.5866	0.706	0.7032	1.64	10.4	0.095	0.5126			−0.68	4.03	705
S3201-26	GNG	364	69.9	203	0.9964	0.709	0.7037	2.56	14.9	0.104	0.5126			−0.76	3.56	765
ZK001-25	DI	298.8	11.6175	657.9	0.0511	0.704	0.7037	1.996	17.47	0.069	0.5128	0.114	0.5127	2.887	7.7512	386
ZK001-350	DI	298.8	8.715	648.6	0.0389	0.704	0.7037	1.968	19.86	0.06	0.5128	0.099	0.5126	2.4969	7.7096	382
ZK001-396	DI	298.8	11.9025	749.4	0.046	0.704	0.7041	3.966	17.23	0.139	0.5128	0.23	0.5125	2.9651	5.1618	739
721-1	GR	307	14.9663	212.8	0.2035	0.705	0.7043	1.443	9.591	0.091	0.5128	0.151	0.5126	2.2823	6.435	493
721-3	GR	307	14.2313	194.2	0.212	0.705	0.7043	2.673	12.85	0.126	0.5127	0.208	0.5125	1.8337	4.6214	727
721-5	GR	307	14.5125	209	0.2009	0.705	0.7043	1.739	12.24	0.086	0.5127	0.142	0.5126	1.9507	6.3017	493

Abbreviation: MG, monzonitic granite; GNG, gneissic granite; DI, diorite; GR, granite. $({}^{87}\text{Sr}/{}^{86}\text{Sr})_i = ({}^{87}\text{Sr}/{}^{86}\text{Sr})_s - ({}^{87}\text{Rb}/{}^{86}\text{Sr})_s \times (e^{\lambda t} - 1)$; ${}^{87}\text{Sr}/{}^{86}\text{Sr} = (\text{Rb}/\text{Sr}) \times 2.8956$; $\lambda_{\text{Rb-Sr}} = 1.42 \times 10^{-11} \text{ a}^{-1}$; $({}^{143}\text{Nd}/{}^{144}\text{Nd})_i = ({}^{143}\text{Nd}/{}^{144}\text{Nd})_s - ({}^{147}\text{Sm}/{}^{144}\text{Nd})_s \times (e^{\lambda t} - 1)$; ${}^{147}\text{Sm}/{}^{144}\text{Nd} = (\text{Sm}/\text{Nd}) \times 0.60456$; $\lambda_{\text{Sm-Nd}} = 6.54 \times 10^{-12} \text{ a}^{-1}$; $\epsilon\text{Nd}(t) = 10,000 [({}^{143}\text{Nd}/{}^{144}\text{Nd})_i / ({}^{143}\text{Nd}/{}^{144}\text{Nd})_{\text{CHUR}(t)} - 1]$; $({}^{143}\text{Nd}/{}^{144}\text{Nd})_{\text{CHUR}(t)} = ({}^{143}\text{Nd}/{}^{144}\text{Nd})_{\text{CHUR}(0)} - ({}^{147}\text{Sm}/{}^{144}\text{Nd})_{\text{CHUR}} \times (e^{\lambda t} - 1)$; $({}^{143}\text{Nd}/{}^{144}\text{Nd})_{\text{CHUR}(0)} = 0.512638$; $({}^{147}\text{Sm}/{}^{144}\text{Nd})_{\text{CHUR}} = 0.1967$; $T_{\text{DM}} = 1/\lambda \cdot \ln\{1 + [({}^{143}\text{Nd}/{}^{144}\text{Nd})_s - ({}^{143}\text{Nd}/{}^{144}\text{Nd})_{\text{DM}}] / [({}^{147}\text{Sm}/{}^{144}\text{Nd})_s - ({}^{147}\text{Sm}/{}^{144}\text{Nd})_{\text{DM}}]\}$; $({}^{147}\text{Sm}/{}^{144}\text{Nd})_{\text{DM}} = 0.21357$; $({}^{143}\text{Nd}/{}^{144}\text{Nd})_{\text{DM}} = 0.51315$; $({}^{147}\text{Sm}/{}^{144}\text{Nd})_{\text{crust}} = 0.118$.

Table 6. Molybdenite Re–Os isotopic data for the Yuhaxi Mo(Cu) deposit.

Sample No.	Weight (g)	Ores Type	Occurrence	Re/ $\mu\text{g}\cdot\text{g}^{-1}$		Os/ $\text{ng}\cdot\text{g}^{-1}$		¹⁸⁷ Re/ $\mu\text{g}\cdot\text{g}^{-1}$		¹⁸⁷ Os/ $\text{ng}\cdot\text{g}^{-1}$		Model Age (Ma)	
				Measured	2σ	Measured	2σ	Measured	2σ	Measured	2σ	Measured	2σ
Mo-01	0.00306	Mo mineralized MG	Dissemination	206.7	1.8	0.0072	0.2	129.9	1.1	741	4.2	341.4	4.9
Mo-02	0.00516	Mo mineralized MG	Dissemination	223.4	3.4	0.0022	0.1	140.4	2.2	793.4	5.8	338.2	6.7

Table 6. Cont.

Sample No.	Weight (g)	Ores Type	Occurrence	$\text{Re}/\mu\text{g}\cdot\text{g}^{-1}$		$\text{Os}/\text{ng}\cdot\text{g}^{-1}$		$^{187}\text{Re}/\mu\text{g}\cdot\text{g}^{-1}$		$^{187}\text{Os}/\text{ng}\cdot\text{g}^{-1}$		Model Age (Ma)	
				Measured	2σ	Measured	2σ	Measured	2σ	Measured	2σ	Measured	2σ
Mo-03	0.00141	Mo mineralized MG	Dissemination	226	1.8	0.008	0.1	142.1	1.2	820.5	5.7	345.7	5.0
Mo-04	0.00311	Mo mineralized MG	Dissemination	411.5	5.0	0.0071	0.2	258.6	3.1	1510.8	9.3	349.6	5.9
Mo-05	0.00205	Mo mineralized MG	Dissemination	204.1	1.8	0.0087	0.3	128.3	1.1	737.7	4.5	344.2	5.0
Mo-06	0.00051	Mo mineralized MG	Dissemination	513.7	5.4	0.0087	0.4	322.9	3.4	1889.2	18.7	350.2	6.1
Mo-07	0.0031	Ccp-Mo-Qz veinlet	Veinlet	330.7	3.2	0.0072	0.2	207.8	2.0	1206.3	7.2	347.4	5.2
Mo-08	0.00509	Ccp-Mo-Qz veinlet	Veinlet	149.3	1.9	0.0023	0.1	93.9	1.2	539.5	3.3	344.1	5.8
Mo-09	0.00511	Ccp-Mo-Qz veinlet	Veinlet	182.6	2.9	0.0021	0.1	114.8	1.8	648	4.0	337.9	6.7

Abbreviation: MG, monzonitic granite. Decay constant: $\lambda^{187}\text{Re} = 1.666 \times 10^{-11} \text{ year}^{-1}$ [46]. Uncertainty in the Re and Os concentrations includes errors associated with the weighing of the sample and diluent, the calibration error of the diluent, the mass spectrometry analytical error, and the measurement error of the isotope ratios for the test sample; the confidence level is 95%. Uncertainty in the Re-Os model ages includes the uncertainty of the ^{187}Re decay constant, with a confidence level of 95%. Uncertainties for ages are absolute (2σ).

5. Discussion

5.1. Timing of Magmatism and Mineralization of Yuhaixi Mo(Cu) Deposit

Multiple magmatic activities were documented in the eastern segment of the Dananhu-Tousuquan island arc belt [25–29]. Our study reveals that at least two stages (~359 Ma and ~307–299 Ma) of magmatic activities occurred in the Yuhaixi area. Zircon U-Pb dating showed that Yuhaixi monzonitic granite, granite, and diorite were emplaced at ~359 Ma, ~307 Ma, and ~299 Ma, respectively. However, other intrusive rocks near the Yuhaixi orefield were reported to form at ~443–430 Ma, earlier than that of Yuhaixi intrusive rocks. For example, Wang et al. (2016) obtained the age of the rocks in the Yuhai Mo(Cu) deposit to be 441.6 ± 2.5 Ma, 430.3 ± 2.6 Ma for the diorite and granodiorite, respectively [5]; Wang et al. (2015) obtained the age of the Sanchakou pluton to be 443 Ma; Wang et al. (2016a) obtained the age of the felsic intrusion in the Sanchakou mining area to be 440–426 Ma [30]; and Wang et al. (2018) obtained the age of the Yuhai quartz diorite to be 443.5 ± 4.1 Ma [12]. Overall, at least three stages of magmatic activities were identified and recorded in the eastern segment of the Dananhu-Tousuquan island arc belt, namely ~430–443 Ma, ~359 Ma, and ~307–299 Ma.

The molybdenite Re-Os dating shows that the Yuhaixi Mo(Cu) deposit was formed at 354 ± 6.8 Ma (Figure 10), which is approximately coeval with the emplaced ages of the Yuhaixi monzonitic granite (359.4 ± 1.6 Ma). Previous studies have shown that the Yuhai molybdenite age [5] and the Sanchakou molybdenite age are concentrated in 370–350 Ma (Figure 11 [30]), which are consistent with the molybdenite Re-Os age of Yuhaixi Mo(Cu) deposit. So, the Yuhaixi Mo(Cu) deposit is suggested to form at ~354–360 Ma. The Yuhaixi granite and diorite rocks are post-ore intrusive plutons. Field investigations revealed that Yuhaixi Mo(Cu) deposits are characterized by disseminated or veinlet ores, and Mo mineralization mainly occurs in the potassic alteration zone (Figure 4I). It is highly likely that the monzonitic granite contributed to the generation of the Yuhaixi deposit.

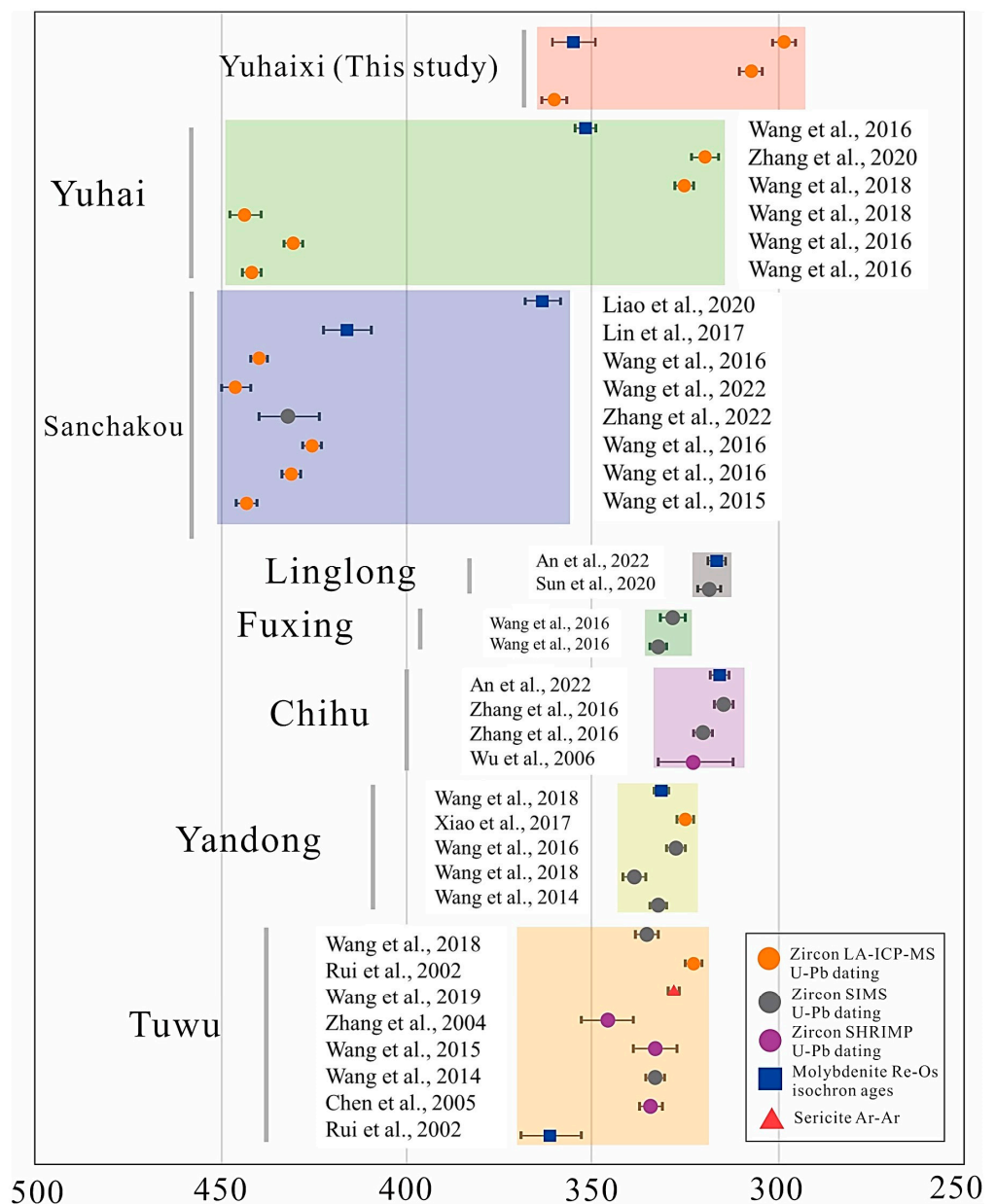


Figure 11. Summary of geochronological data of major porphyry Cu deposits in the Eastern-Tianshan. Error bars are 2σ [5–7,9,12,47–58].

5.2. Petrogenesis

The Yuhai monzonitic granite is characterized by high SiO_2 and $\text{K}_2\text{O} + \text{Na}_2\text{O}$ contents, low Al_2O_3 content, and the depletion of aluminum-rich minerals (e.g., muscovite, tourmaline, and garnet). They have a weak peraluminous character ($1 < A/\text{CNK} < 1.1$), and they exhibit low Sr (< 188 ppm) and Y contents with relatively low Sr/Y ratios (< 25). These features suggest that the Yuhai intrusion can be classified as the I- or A-type granite [21]. In addition, the Yuhai monzonitic granite shows low $\text{FeOt}/(\text{FeOt} + \text{MgO})$ ratios, Zr content, and $10^4 \times \text{Ga}/\text{Al}$ ratios (2.1–2.4), excluding the possibility of A-type granite (Figure 8d). Therefore, the Yuhai monzonitic granite likely belongs to I-type granites [59]. The Yuhai post-ore granite is a high silica granite and exhibits similar geochemical signatures to the causative monzonitic granite. The Yuhai post-ore granite also has relatively low A/CNK (< 1.1) and Ga/Al ratios, which is consistent with the features of I-type granites.

Generally, the $Mg^\#$ values of magmatic rocks formed by the partial melting of the basaltic lower crust are less than 40 regardless of the degree of melting [43,44,60]. If mantle material was involved in the origin of ore-forming felsic rocks, $Mg^\#$ values of these rocks will be higher than 40 [60]. Thus, the $Mg^\#$ values can be used as an important indicator to track the addition of mantle-derived magma. Overall, the Yuhaxi felsic rocks both show high silica and low MgO, Cr, Ni contents, which is in favor of the crust origin. They both are enriched in LREE and LILE and depleted in HFSE elements (e.g., Nb, Ta) in the primitive mantle-normalized diagram (Figure 9). The Yuhaxi monzonitic granite samples have significant variable $^{87}Sr/^{86}Sr$ ratios, ranging from 0.7041–0.7127, and high $\epsilon_{Hf}(t)$ (11.37–17.59) and $\epsilon_{Nd}(t)$ (1.36–3.4) values, suggesting that it may have formed by melting the juvenile crust with the involvement of crustal components [43–45,60]. In addition, the Yuhaxi monzonitic granite is high silica granite and is lithologically homogeneous, arguing against the significant upper crustal contamination and fractional crystallization of basaltic magmas [40]. The studied monzonitic granite is characterized by high K_2O (3.8–5.0 wt.%) and K_2O/Na_2O (1.1–1.6) ratios and shows relatively low Rb/Sr (0.34–0.47) and high K/Rb (396–615) ratios without obvious Eu-negative anomaly, indicating that it is less evolved than high-K granites. Thus, we proposed that Yuhaxi monzonitic granite likely originated from the partial melting of the juvenile lower crust with the involvement of hydrous melts or fluids sourced from continental crustal components (e.g., subducting sediments). However, Yuhaxi post-ore granite shows high Na_2O (4.5–4.6 wt.%) contents and low K_2O/Na_2O (~0.6) ratios and it has low initial $^{87}Sr/^{86}Sr$ ratios (0.7042–0.7043) but high $\epsilon_{Hf}(t)$ (11.7–14.8) and $\epsilon_{Nd}(t)$ (4.6–6.4) values, which suggests that Yuhaxi granite likely originated from the partial melting of the juvenile crust with the addition of ocean crustal components (e.g., subducting oceanic slab) [45].

Compared to the Yuhaxi felsic rocks, Yuhaxi diorites have relatively low silica (53–54 wt.%) and high MgO (4.1–5.1 wt.%), Na_2O (3.9–4.1 wt.%), and Al_2O_3 (17.3–18 wt.%) contents with high Cr, V, and Ni contents. Their high MgO ($Mg^\# > 45$) and high transition metal (e.g., Cr, Ni, V) contents suggest the Yuhaxi high-Al diorites may be derived from the depleted lithospheric mantle source [20,23,25]. They have relatively low initial $^{87}Sr/^{86}Sr$ ratios, and high $\epsilon_{Nd}(t)$ (5.16–7.75) and $\epsilon_{Hf}(t)$ values (11.59–13.46), further supporting the depleted mantle origin. However, the Yuhaxi diorite samples are enriched in LREEs and LILEs, depleted in HREEs and HFSEs, and exhibit high Sr contents (785–941 ppm), Ba/La, Ba/Th ratios, but low Th/Yb, and Th/Nb ratios. Plank and Langmuir (1998) pointed out that the magma formed from the source area metasomatized by the slab dehydration fluid usually has high Sr, Ba content and Ba/Th ratio (>170) [45]. Therefore, the Yuhaxi diorite is likely derived from partial melting of the metasomatized mantle wedge (Figure 12) [31].

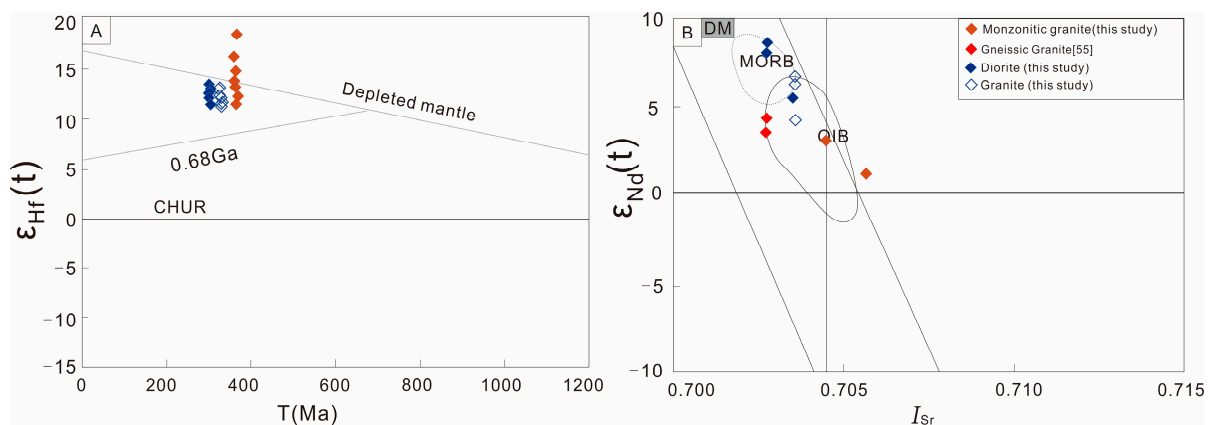


Figure 12. (A) Zircon $\epsilon_{Hf}(t)$ vs. U-Pb ages (T) diagram for the Yuhaxi intrusions. (B) $\epsilon_{Nd}(t)$ vs. I_{Sr} diagram for the Yuhaxi intrusions.

In a word, the Yuhaixi felsic intrusive rocks are high silica ($\text{SiO}_2 > 70$ wt.%) and are characterized by high total alkali and low MgO, Cr, Ni contents and high $\epsilon\text{Nd}(t)$ and $\epsilon\text{Hf}(t)$ values. These characteristics suggest that their melts are mainly derived from the partial melting of the juvenile lower crust. However, the post-ore diorite has a feature of high Al_2O_3 , Na_2O contents with depleted isotopic signatures, indicating that diorite melts likely originated from the partial melting of depleted lithospheric mantle metasomatized by fluids or hydrous melts from the subducting slabs [5,9,12,21,23].

5.3. Implication for Tectonic Evolution and Porphyry Mineralization in Eastern Tianshan

The tectonic evolution of the Dananhu-Tousuquan arc belt has been widely addressed in previous studies [5,12,27–29], and a growing number of Paleozoic arc-related magmatic rocks have been reported in the Dananhu-Tousuquan island arc belt [11–16,25–30]. As reflected by the tectonic discrimination diagrams (Figure 13), Yuhaixi intrusive rocks including felsic and intermediate rocks all fall within the volcanic arc granitoid field, suggesting that they were formed in a subduction tectonic setting during Paleozoic era. Stratigraphic [29] and tectonic [30] studies indicated that the early Paleozoic Dananhu-Tousuquan island arcs were formed by the N-dipping subduction of the North Tianshan oceanic plate [5,12,27,29]. In the early Paleozoic, the partial melting of the low-angle, young subducted North Tianshan oceanic slab probably generated the Sanchakou adakite rocks (ca. 443 Ma–430 Ma; Unpublished data) (Figure 14A). The Carboniferous bipolar subduction of the North Tianshan Ocean formed the major Dananhu-Tousuquan island arc belt to the north and the Aqishan-Yamansu arc belt to the south (Figure 14B; [9,27,34–36,40]). During this period, asthenosphere upwelling triggered by the roll back or retraction of the subduction plate resulted in the partial melting of the juvenile lower crust to generate the Yuhaixi monzonitic granite (~360 Ma; Figure 14B). Meanwhile, with the emplacement of these magmas, the arc-related porphyry Mo mineralization was formed in the Dananhu-Tousuquan island arc belt (Figure 14B). The Eastern Tianshan bimodal magmatism, e.g., the Baiyanggou gabbro (295.8 ± 2.8 Ma) and rhyolite (293 ± 1.7 Ma) [61,62], the Cheguluquan rhyolite (294.5 ± 3.6 Ma) and basalt (293.6 ± 2.3 Ma) [63], and the youngest Hongshishan ophiolite in this belt (~310 Ma), suggest that the Eastern Tianshan tectonic setting was dominated by extension, which implies that the collision between the Dananhu-Tousuquan and Aqishan-Yamansu belts likely occurred during the late Carboniferous to early Permian periods [38,41]. This idea is also favored by the occurrence of diorite (298.0 ± 1.8 Ma) and granite (307.0 ± 2.3 Ma) in the Yuhaixi area. Moreover, many extension-related magmatic Cu-Ni sulfide deposits that occurred in the post-collisional setting were documented and reported in ca. 300–275 Ma [64], which also support the view of the collision between the Dananhu-Tousuquan and Aqishan-Yamansu belts [65–67].

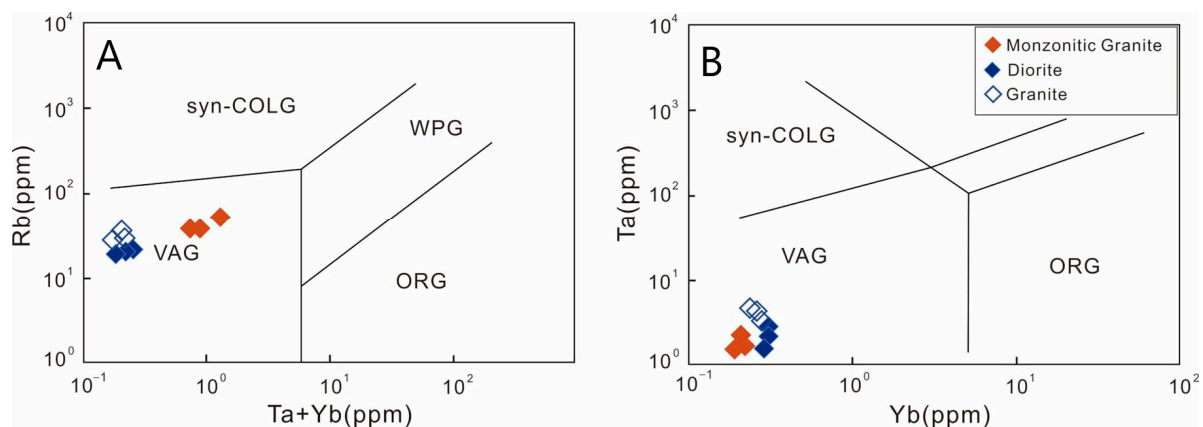


Figure 13. Tectonic discrimination diagrams for the Yuhaixi intrusions. (A) Rb vs. Ta + Yb diagram [33]; (B) Ta vs. Yb diagram [33]. Syn-COLG = Syn-collision granites; WPG = Within plate granites; ORG = Ocean ridge granites; VAG = Volcanic arc granites.

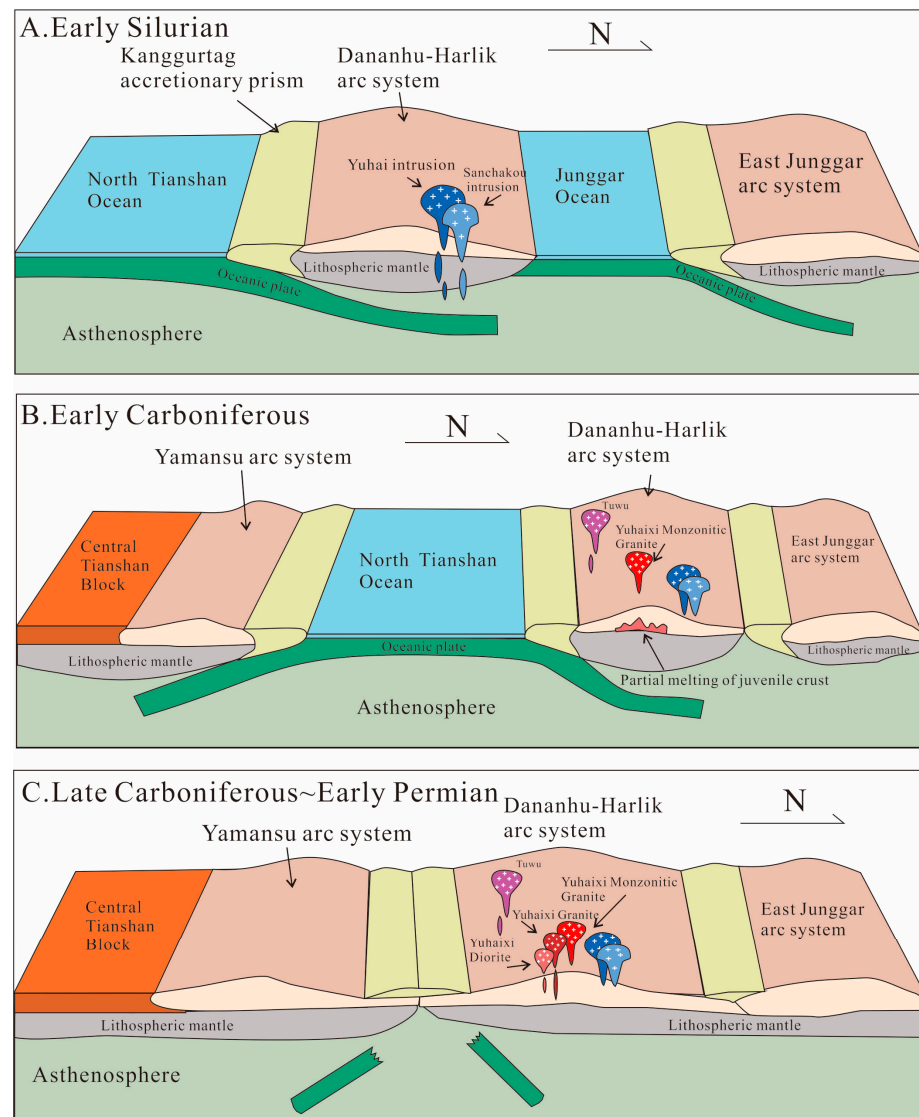


Figure 14. Schematic cartoons illustrating the tectono–magmatic–metallogenic evolution model of the Yuhaxi porphyry Mo(Cu) deposit in eastern Tianshan. (A) N-dipping subduction of the North Tianshan ocean plate gave rise to the Bogeda-Haerlike and Dananhu-Tousuquan island arcs in the early Paleozoic period. (B) Bipolar subduction of the North Tianshan ocean plate gave rise to the Dananhu-Tousuquan and Aqishan-Yamansu arcs in the Carboniferous period, forming Yuhaxi monzonitic granite and granite. (C) The Permian period post-collisional extension forming Yuhaxi diorite.

6. Conclusions

- (1) Zircon LA-ICP-MS U-Pb dating suggests that the emplaced ages of the Yuhaxi monzonitic granite, diorite, and granite are 359.4 ± 1.6 Ma, 298.8 ± 1.8 Ma, and 307.0 ± 2.3 Ma, respectively.
- (2) The Re-Os dating of molybdenite hosted by Yuhaxi monzonitic granite yields a well-constrained ^{187}Re – ^{187}Os isochron age of 354.1 ± 6.8 Ma (MSWD = 1.7).
- (3) Whole-rock geochemical characteristics and Sr-Nd-Hf isotopic compositions indicate that the Yuhaxi monzonitic granite and granite were formed via the partial melting of the juvenile crust. The post-ore diorite was formed via the partial melting of the metasomatized mantle wedge.
- (4) The eastern section of the Dananhu-Tousuquan island arc is a promising target for late Paleozoic porphyry Mo(Cu) deposits.

Author Contributions: Conceptualization, D.W. and C.X.; investigation, D.W., Y.Z., C.X., B.X., Y.Y., Q.T., X.K. and X.W.; methodology, D.W., C.L. and C.X.; data curation, D.W. and C.L.; writing—original draft preparation, D.W.; writing—review and editing, D.W., Y.Z. and C.X.; supervision, C.X.; funding acquisition, C.X., C.L. and Y.Z.; Resources, X.K. All authors have read and agreed to the published version of the manuscript.

Funding: This research was funded by the National Key R&D Program of China (2017YFC0601202 and 2020YFA0714800) and Open Research Project from the State Key Laboratory of Geological Processes and Mineral Resources (GPMR202307). Chunji Xue acknowledges funding under the Xinjiang Uygur Autonomous Region Introduced Project “Tianchi talent”.

Data Availability Statement: All data are presented in the paper.

Acknowledgments: The authors would like to thank the managers and geological staff of No. 1 Geological Team of Xinjiang for their support with the fieldwork. The authors are also deeply grateful for the reviews and constructive suggestions of the anonymous reviewers.

Conflicts of Interest: The authors declare no conflict of interest.

References

- Sillitoe, R.H. Porphyry copper systems. *Econ. Geol.* **2010**, *105*, 3–41. [\[CrossRef\]](#)
- Sinclair, W.D. Porphyry deposits. Mineral Deposits of Canada: A Synthesis of Major Deposit-Types, District Metallogeny, the Evolution of Geological Provinces, and Exploration Methods. In *Geological Association of Canada, Mineral Deposits Division, Special Publication No. 5*; Geological Association of Canada: St. John's, NL, Canada, 2007; pp. 223–243.
- Gao, J.; Klemd, R.; Zhu, M.; Wang, X.-S.; Li, J.; Wan, B.; Xiao, W.; Zeng, Q.; Shen, P.; Sun, J.; et al. Large-scale porphyry-type mineralization in the Central Asian metallogenic domain: A review. *J. Asian Earth Sci.* **2018**, *165*, 7–36. [\[CrossRef\]](#)
- Yan, D.-P.; Qiu, L. Geology of China and adjacent regions: An introduction. *J. Asian Earth Sci.* **2020**, *203*, 104533. [\[CrossRef\]](#)
- Wang, Y.; Zhang, F.; Liu, J. The genesis of the ores and intrusions at the Yuhai Cu-Mo deposit in eastern Tianshan, NW China: Constraints from geology, geochronology, geochemistry, and Hf isotope systematics. *Ore Geol. Rev.* **2016**, *77*, 312–331. [\[CrossRef\]](#)
- Xiao, B.; Chen, H.; Hollings, P.; Han, J.; Wang, Y.; Yang, J.; Cai, K. Magmatic evolution of the Tuwu–Yandong porphyry Cu belt, NW China: Constraints from geochronology, geochemistry and Sr–Nd–Hf isotopes. *Gondwana Res.* **2017**, *43*, 74–91. [\[CrossRef\]](#)
- Wang, Y.H.; Zhang, F.F.; Liu, J.J.; Que, C.Y. Genesis of the Fuxing porphyry Cu deposit in Eastern Tianshan, China: Evidence from fluid inclusions and C–H–O–S–Pb isotope systematics. *Ore Geol. Rev.* **2016**, *79*, 46–61. [\[CrossRef\]](#)
- Zhang, H.; Qiu, L.; Yan, D.-P.; Zhao, Z.; Cai, K.; Zhang, J.; Chen, S.; Li, Y.; Song, Y.; Zheng, Y.; et al. Late-Permian subduction-to-collision transition and closure of Paleo-Asian Ocean in eastern Central Asian Orogenic Belt: Evidence from borehole cores in the Songliao Basin, Northeast China. *Gondwana Res.* **2023**, *122*, 74–92. [\[CrossRef\]](#)
- Zhang, F.; Wang, Y.; Liu, J. Petrogenesis of Late Carboniferous granitoids in the Chihu area of Eastern Tianshan, Northwest China, and tectonic implications: Geochronological, geochemical, and zircon Hf–O isotopic constraints. *Int. Geol. Rev.* **2016**, *58*, 949–966. [\[CrossRef\]](#)
- Wang, Y.; Chen, H.; Baker, M.J.; Han, J.; Xiao, B.; Yang, J.; Jourdan, F. Multiple mineralization events of the Paleozoic Tuwu porphyry copper deposit, Eastern Tianshan: Evidence from geology, fluid inclusions, sulfur isotopes, and geochronology. *Miner. Depos.* **2018**, *54*, 1053–1076. [\[CrossRef\]](#)
- Xiao, B.; Chen, H.; Wang, Y.; Han, J.; Xu, C.; Yang, J. Chlorite and epidote chemistry of the Yandong Cu deposit, NW China: Metallogenic and exploration implications for Paleozoic porphyry Cu systems in the Eastern Tianshan. *Ore Geol. Rev.* **2018**, *100*, 168–182. [\[CrossRef\]](#)
- Wang, Y.F.; Chen, H.Y.; Han, J.S. Paleozoic tectonic evolution of the Dananhu-Tousuquan island arc belt, Eastern Tianshan: Constraints from the miaoagmatism of the Yuhai porphyry Cu deposit, Xinjiang, NW China. *J. Asian Earth Sci.* **2018**, *153*, 282–306. [\[CrossRef\]](#)
- Xiao, W.; Windley, B.F.; Allen, M.B.; Han, C. Paleozoic multiple accretionary and collisional tectonics of the Chinese Tianshan orogenic collage. *Gondwana Res.* **2013**, *23*, 1316–1341. [\[CrossRef\]](#)
- Sun, H.; Li, H.; Danišik, M.; Xia, Q.; Jiang, C.; Wu, P.; Yang, H.; Fan, Q.; Zhu, D. U–Pb and Re–Os geochronology and geochemistry of the Donggebi Mo deposit, Eastern Tianshan, NW China: Insights into mineralization and tectonic setting. *Ore Geol. Rev.* **2017**, *86*, 584–599. [\[CrossRef\]](#)
- Zhang, S.; Chen, H.; Hollings, P.; Zhao, L.; Gong, L. Tectonic and magmatic evolution of the Aqishan–Yamansu belt: A Paleozoic arc-related basin in the Eastern Tianshan (NW China). *GSA Bull.* **2020**, *133*, 1320–1344. [\[CrossRef\]](#)
- Hou, G.S.; Tang, H.F.; Liu, C.Q.; Wang, Y.B. Geochronological and geochemical study on the wallrock of Tuwu–Yandong porphyry copper deposits, eastern Tianshan mountains. *Acta Petrol. Sin.* **2005**, *21*, 1729–1736.
- Ballard, R.J.; Palin, M.J.; Campbell, I.H. Relative oxidation states of magmas inferred from Ce (IV)/Ce (III) in zircon: Application to porphyry copper deposits of northern Chile. *Contrib. Mineral. Petrol.* **2002**, *144*, 347–364. [\[CrossRef\]](#)
- Elhlou, S.; Belousova, E.; Griffin, W.; Pearson, N.; O'Reilly, S. Trace element and isotopic composition of GJ-red zircon standard by laser ablation. *Geochim. Cosmochim. Acta* **2006**, *70*, A158. [\[CrossRef\]](#)

19. Liang, Q.; Jing, H.; Gregoire, D.C. Determination of trace elements in granites by inductively coupled plasma mass spectrometry. *Talanta* **2000**, *51*, 507–513. [[CrossRef](#)]
20. Sun, S.S.; McDonough, W.F. Chemical and isotopic systematics of oceanic basalts: Implications for mantle composition and processes. In *Magmatism in the Ocean Basin*; Geological Society Special Publication: London, UK, 1989; Volume 42, pp. 313–345.
21. Hoskin, P.W.O.; Schaltegger, U. The composition of zircon and igneous and metamorphic petrogenesis. *Rev. Mineral. Geochem.* **2003**, *53*, 27–62. [[CrossRef](#)]
22. Ferry, J.M.; Watson, E.B. New thermodynamic models and revised calibrations for the Ti-in-zircon and Zr-in-rutile thermometers. *Contrib. Mineral. Petrol.* **2007**, *154*, 429–437. [[CrossRef](#)]
23. Blichert-Toft, J.; Albarède, F. The Lu-Hf isotope geochemistry of chondrites and the evolution of the mantle-crust system. *Earth Planet. Sci. Lett.* **1997**, *148*, 243–258.
24. Griffin, W.L.; Pearson, N.J.; Belousova, E.; Jackson, S.V.; Van Acherbergh, E.; O'Reilly, S.Y.; Shee, S.R. The Hf isotope composition of cratonic mantle: LAM-MC-ICPMS analysis of zircon megacrysts in kimberlites. *Geochim. Cosmochim. Acta* **2000**, *64*, 133–147. [[CrossRef](#)]
25. Chen, F.W.; Li, H.Q.; Chen, Y.C.; Wang, D.H.; Wang, J.L.; Liu, D.Q.; Zhou, R.H. Zircon SHRIMP U–Pb dating and its geological significance of mineralization in Tuwu-Yandong porphyry copper mine, East Tianshan Mountain. *Acta Geol. Sin.* **2005**, *79*, 256–261.
26. Wu, H.; Li, H.Q.; Chen, F.W.; Lu, Y.F.D.; Mei, Y.P. Zircon SHRIMP U–Pb dating of plagiogranite porphyry in the Chihu molybdenum-copper district, Hami, East Tianshan. *Geol. Bull. China* **2006**, *25*, 549–552.
27. Du, L.; Yuan, C.; Li, X.-P.; Zhang, Y.; Huang, Z.; Long, X. Petrogenesis and Geodynamic Implications of the Carboniferous Granitoids in the Dananhu Belt, Eastern Tianshan Orogenic Belt. *J. Earth Sci.* **2019**, *30*, 1243–1252. [[CrossRef](#)]
28. Rui, Z.Y. Discussion on metallogenic epoch of Tuwu and Yandong porphyry copper deposits in eastern Tianshan Mountains, Xinjiang. *Miner. Depos.* **2002**, *21*, 16–22.
29. Zhang, L.; Qin, K.; Xiao, W. Multiple mineralization events in the eastern Tianshan district, NW China: Isotopic geochronology and geological significance. *J. Southeast Asian Earth Sci.* **2008**, *32*, 236–246. [[CrossRef](#)]
30. Wang, Y.-H.; Zhang, F.-F. Petrogenesis of early Silurian intrusions in the Sanchakou area of Eastern Tianshan, Northwest China, and tectonic implications: Geochronological, geochemical, and Hf isotopic evidence. *Int. Geol. Rev.* **2016**, *58*, 1294–1310. [[CrossRef](#)]
31. Wood, D.A. The application of a Th–Hf–Ta diagram to problems of tectonomagmatic classification and to establishing the nature of crustal contamination of basaltic lavas of the British Tertiary Volcanic Province. *Earth Planet. Sci. Lett.* **1980**, *50*, 11–30. [[CrossRef](#)]
32. Du, L.; Zhu, H.; Yuan, C.; Zhang, Y.; Huang, Z.; Li, X.-P.; Long, X. Paleozoic crustal evolution and tectonic switching in the Northeastern Tianshan: Insights from zircon Hf isotopes of granitoids. *J. Geol. Soc.* **2020**, *178*, jgs2020-035. [[CrossRef](#)]
33. Pearce, J.A.; Harris, N.B.W.; Tindle, A.G. Trace Element Discrimination Diagrams for the Tectonic Interpretation of Granitic Rocks. *J. Pet.* **1984**, *25*, 956–983. [[CrossRef](#)]
34. Harris, N.B.W.; Pearce, J.A.; Tindle, A.G. Geochemical characteristics of collision-zone magmatism. In *Geological Society; Special Publications*: London, UK, 1986; Volume 19, pp. 67–81.
35. Zhang, Z.; Ding, H.; Dong, X.; Tian, Z. Partial melting of subduction zones. *Acta Petrol. Sin.* **2020**, *36*, 2589–2615.
36. Tang, G.; Wang, Q.; Wyman, D.A.; Li, Z.-X.; Zhao, Z.-H.; Jia, X.-H.; Jiang, Z.-Q. Ridge subduction and crustal growth in the Central Asian Orogenic Belt: Evidence from Late Carboniferous adakites and high-Mg diorites in the western Junggar region, northern Xinjiang (west China). *Chem. Geol.* **2010**, *277*, 281–300. [[CrossRef](#)]
37. Li, J.Y. Late Neoproterozoic and Paleozoic tectonic framework and evolution of Eastern Xinjiang, NW China. *Geol. Rev.* **2004**, *50*, 304–322, (In Chinese with English Abstract).
38. Liu, Y.; Hu, Z.; Zong, K.; Gao, C.; Gao, S.; Xu, J.; Chen, H. Reappraisal and refinement of zircon U–Pb isotope and trace element analyses by LA–ICP–MS. *Chin. Sci. Bull.* **2010**, *55*, 1535–1546. [[CrossRef](#)]
39. Ludwig, K.R. *Isoplot/Ex, Version 3: A Geochronological Toolkit for Microsoft Excel: Berkley*; Berkeley Geochronology Center: Berkeley, CA, USA, 2003.
40. Tang, G.-J.; Wang, Q.; Wyman, D.A.; Li, Z.-X.; Zhao, Z.-H.; Yang, Y.-H. Late Carboniferous high $\epsilon\text{Nd}(t)$ – $\epsilon\text{Hf}(t)$ granitoids, enclaves and dikes in western Junggar, NW China: Ridge-subduction-related magmatism and crustal growth. *Lithos* **2012**, *140–141*, 86–102. [[CrossRef](#)]
41. Andao, D.; Hongliao, H.; Ningwan, Y.; Xiaoqiu, Z.; Yali, S.; Dezhong, S.; Shaozhen, C.; Wenjun, Q. A Study of the Rhenium Osmium Geochronometry of Molybdenites. *Acta Geol. Sin. Engl. Ed.* **1995**, *8*, 171–181. [[CrossRef](#)]
42. Qu, W.J. Highly precise Re–Os dating of molybdenite by ICP–MS with Carius tube sample digestion. *Rock Miner. Anal.* **2003**, *22*, 254–257.
43. Wang, Q.; Xu, J.-F.; Jian, P.; Bao, Z.-W.; Zhao, Z.-H.; Li, C.-F.; Xiong, X.-L.; Ma, J.-L. Petrogenesis of Adakitic Porphyries in an Extensional Tectonic Setting, Dexing, South China: Implications for the Genesis of Porphyry Copper Mineralization. *J. Pet.* **2005**, *47*, 119–144. [[CrossRef](#)]
44. Liu, S.-A.; Li, S.; He, Y.; Huang, F. Geochemical contrasts between early Cretaceous ore-bearing and ore-barren high-Mg adakites in central-eastern China: Implications for petrogenesis and Cu–Au mineralization. *Geochim. Cosmochim. Acta* **2010**, *74*, 7160–7178. [[CrossRef](#)]

45. Plank, T.; Langmuir, C.H. The chemical composition of subducting sediment and its consequences for the crust and mantle. *Chem. Geol.* **1998**, *145*, 325–394. [[CrossRef](#)]
46. Smoliar, M.I.; Walker, R.J.; Morgan, J.W. Re-Os ages of group IIA, IIIA, IVA, and IVB iron meteorites. *Science* **1996**, *271*, 1099–1102. [[CrossRef](#)]
47. Zhang, W.; Zhang, F.F.; Wang, Y.H.; Xue, C.J.; Wang, J.P.; Sun, M.; Wang, K. Origin of Paleozoic granitoids in the Yuhai Cu–Mo deposit, Eastern Tianshan, NW China and implications for regional metallogeny. *Ore Geol. Rev.* **2020**, *121*, 103465. [[CrossRef](#)]
48. Liao, K.L.; Lyu, C.L. The geological significance of molybdenite Re-Os isotopic dating result of Sanchakouxi Cu deposit in East Tianshan, Xinjiang. *Miner. Resour. Geol.* **2020**, *34*, 471–476, (In Chinese with English Abstract).
49. Lin, T.; Deng, Y.F.; Qu, W.J.; Zhou, T.F.; Yuan, F.; Deng, G. The genesis, petrology, chronology and geochemical evidence of the Sanchakou copper deposit in the East Tianshan area, Xinjiang. *J. Mineral. Petrol.* **2017**, *37*, 47–61, (In Chinese with English Abstract).
50. Wang, Y.; Chen, H.; Falloon, T.J.; Han, J. The Paleozoic-Mesozoic magmatic evolution of the Eastern Tianshan, NW China: Constraints from geochronology and geochemistry of the Sanchakou intrusive complex. *Gondwana Res.* **2022**, *103*, 1–22. [[CrossRef](#)]
51. Zhang, F.F.; Wang, Y.H.; Liu, J.J.; Xue, C.J.; Wang, J.P.; Zhang, W.; Li, Y.Y. Paleozoic magmatism and mineralization potential of the Sanchakou copper deposit, eastern Tianshan, Northwest China: Insights from geochronology, mineral chemistry, and isotopes. *Econ. Geol.* **2022**, *117*, 165–194. [[CrossRef](#)]
52. Wang, C.; Chen, B.; Ma, X.H.; Yan, X.L. Petrogenesis of Early and late Paleozoic Plutons in Sanchakou Area of East Tianshan and Their Implications for Evolution of Kangur Suture Zone. *J. Earth Sci. Environ.* **2015**, *37*, 5.
53. An, W.; Xue, C.; Zhao, Y.; Chao, L. Two Periods of Porphyry Cu Mineralization and Metallogenic Implications in the Tuwu–Yandong Belt (NW China), Based on Re–Os Systematics of Molybdenite. *Minerals* **2022**, *12*, 1127. [[CrossRef](#)]
54. Sun, M.; Wang, Y.H.; Zhang, F.F.; Lin, S.Y.; Xue, C.J.; Liu, J.J.; Zhu, D.C.; Wang, K.; Zhang, W. Petrogenesis of Late Carboniferous intrusions in the Linglong area of Eastern Tianshan, NW China, and tectonic implications: Geochronological, geochemical, and zircon Hf–O isotopic constraints. *Ore Geol. Rev.* **2020**, *120*, 103462. [[CrossRef](#)]
55. Wang, Y.; Chen, H.; Xiao, B.; Han, J.; Fang, J.; Yang, J.; Jourdan, F. Overprinting mineralization in the Paleozoic Yandong porphyry copper deposit, Eastern Tianshan, NW China—Evidence from geology, fluid inclusions and geochronology. *Ore Geol. Rev.* **2018**, *100*, 148–167. [[CrossRef](#)]
56. Shen, P.; Pan, H.; Dong, L. Yandong porphyry Cu deposit, Xinjiang, China—geology, geochemistry and SIMS U–Pb zircon geochronology of host porphyries and associated alteration and mineralization. *J. Asian Earth Sci.* **2014**, *80*, 197–217. [[CrossRef](#)]
57. Zhang, L.; Qin, K.Z.; Ying, J.F.; Xia, B. The relationship between ore-forming processes and adakitic rock in Tuwu–Yandong porphyry copper metallogenic belt, eastern Tianshan mountains. *Acta Petrol. Sin.* **2004**, *20*, 259–268.
58. Wang, Y.H.; Xue, C.J.; Liu, J.J.; Wang, J.P.; Yang, J.T.; Zhang, F.F.; Zhao, Z.N.; Zhao, Y.J.; Liu, B. Early Carboniferous adakitic rocks in the area of the Tuwu deposit, eastern Tianshan, NW China: Slab melting and implications for porphyry copper mineralization. *J. Asian Earth Sci.* **2015**, *103*, 332–349. [[CrossRef](#)]
59. Whalen, J.B.; Currie, K.L.; Chappell, B.W. A-type granites: Geochemical characteristics, discrimination and petrogenesis. *Contrib. Mineral. Petr.* **1987**, *95*, 407–419. [[CrossRef](#)]
60. Richards, J.P.; Kerrich, R. Special Paper: Adakite-Like Rocks: Their Diverse Origins and Questionable Role in Metallogenesis. *Econ. Geol.* **2007**, *102*, 537–576. [[CrossRef](#)]
61. Chen, X.; Shu, L.; Santosh, M.; Zhao, X. Island arc-type bimodal magmatism in the eastern Tianshan Belt, Northwest China: Geochemistry, zircon U–Pb geochronology and implications for the Paleozoic crustal evolution in Central Asia. *Lithos* **2013**, *168–169*, 48–66. [[CrossRef](#)]
62. Chen, X.; Shu, L.; Santosh, M. Late Paleozoic post-collisional magmatism in the Eastern Tianshan Belt, Northwest China: New insights from geochemistry, geochronology and petrology of bimodal volcanic rocks. *Lithos* **2011**, *127*, 581–598. [[CrossRef](#)]
63. Yuan, C.; Sun, M.; Wilde, S.; Xiao, W.; Xu, Y.; Long, X.; Zhao, G. Post collisional plutons in the Balikun area, East Chinese Tianshan: Evolving magmatism in response to extension and slab break-off. *Lithos* **2010**, *119*, 269–288. [[CrossRef](#)]
64. Qiu, M.; Zhao, Y.; Xue, C.; Chen, J.; Ma, X.; Wang, L.; Yu, L.; You, Y. genesis of the Ni–Cu sulfide mineralization of the carboniferous Haibaotan intrusion, Eastern Tianshan, Central Asian Orogenic Belt. *Int. J. Earth Sci.* **2022**, *112*, 1–26. [[CrossRef](#)]
65. Rickwood, P.C. Boundary lines within petrologic diagrams which use oxides of major and minor elements. *Lithos* **1989**, *22*, 247–263. [[CrossRef](#)]
66. Irvine, T.N.; Baragar, W.R.A. A Guide to the Chemical Classification of the Common Volcanic Rocks. *Can. J. Earth Sci.* **1971**, *8*, 523–548. [[CrossRef](#)]
67. Huang, B.; Chen, S.; Li, C.; Tian, Q.; Wang, C.; Wu, J.; Chen, M.; Han, J.; Wang, Y. Geochemical Features and Geological Significance of Yuhai Plutons in Eastern Tianshan, Xinjiang. *Earth Sci.* **2018**, *43*, 2943–2965.

Disclaimer/Publisher’s Note: The statements, opinions and data contained in all publications are solely those of the individual author(s) and contributor(s) and not of MDPI and/or the editor(s). MDPI and/or the editor(s) disclaim responsibility for any injury to people or property resulting from any ideas, methods, instructions or products referred to in the content.